

Simulating the processes controlling ice-shelf rift paths using damage mechanics

Alex Huth^{1,4}, Ravindra Duddu², Benjamin Smith³, and Olga Sergienko⁴

¹NOAA/GFDL, Princeton, NJ, USA

²Department of Civil and Environmental Engineering, Vanderbilt University, Nashville, TN, USA

³Applied Physics Laboratory, Polar Science Center, University of Washington, Seattle, WA, USA

⁴Atmospheric and Oceanic Sciences, Princeton University, Princeton, NJ, USA

Correspondence: Alex Huth <Alexander.Huth@noaa.gov>

This is the preprint of an article that has been submitted for publication in the Journal of Glaciology.
It has not been peer-reviewed.

1 Simulating the processes controlling ice-shelf rift paths 2 using damage mechanics

3 Alex HUTH,^{1,4} Ravindra DUDDU,² Benjamin SMITH,³ Olga SERGIENKO⁴

4 ¹ *NOAA/GFDL, Princeton, NJ, USA*

5 ² *Department of Civil and Environmental Engineering, Vanderbilt University, Nashville, TN, USA*

6 ³ *Applied Physics Laboratory, Polar Science Center, University of Washington, Seattle, WA, USA*

7 ⁴ *Atmospheric and Oceanic Sciences, Princeton University, Princeton, NJ, USA*

8 *Correspondence: Alex Huth <Alexander.Huth@noaa.gov>*

9 **ABSTRACT.**

10 **Rifts are full-thickness fractures that propagate laterally across the ice shelf.**
11 **They cause ice-shelf weakening and calving of tabular icebergs, and control**
12 **the initial size of calved icebergs. Here, we present a combined inverse and**
13 **forward computational modeling framework to capture rifting by combining**
14 **the vertically integrated momentum balance and anisotropic continuum dam-**
15 **age mechanics formulations. We incorporate rift-flank boundary processes to**
16 **investigate how the rift path is influenced by the pressure on rift-flank walls**
17 **from seawater, contact between flanks, and ice mélange that may also trans-**
18 **mit stress between flanks. To illustrate the viability of the framework, we**
19 **simulate the final two years of rift propagation associated with the calving**
20 **of tabular iceberg A68 in 2017. We find that the rift path can change with**
21 **varying ice mélange conditions and the extent of contact between rift flanks.**
22 **Combinations of parameters associated with slower rift widening rates yield**
23 **simulated rift paths that best match observations. Our modeling framework**
24 **lays the foundation for robust simulation of rifting and tabular calving pro-**
25 **cesses, which can enable future studies on ice-sheet–climate interactions, and**
26 **the effects of ice-shelf buttressing on land ice flow.**

1 INTRODUCTION

Ice-shelf rifting weakens ice shelves and precedes calving of tabular icebergs, which comprise the vast majority of calved Antarctic ice volume (Tournadre and others, 2016). Calving and submarine melting are the two major causes of the recent Antarctic losses of ice-shelf mass and buttressing of upstream grounded ice (Greene and others, 2022). Decreased buttressing can affect the discharge of grounded ice into the ocean and ice-sheet contribution to sea-level rise (Haseloff and Sergienko, 2022), and calved icebergs can transport freshwater to lower latitudes to influence ocean circulation and sea-ice growth (e.g. Jongma and others, 2009; Martin and Adcroft, 2010; Merino and others, 2016), as well as the marine biosphere (e.g. Arrigo and others, 2002; Laufkötter and others, 2018).

The processes that control rifting are poorly-understood, and it remains a challenge to capture rifting within computer simulations of ice shelf evolution. Past observational evidence and modeling suggest that rifting is primarily driven by viscous, glaciological stresses associated with gravity-driven ice flow (e.g. Joughin and MacAyeal, 2005; Bassis and others, 2005, 2007, 2008; Borstad and others, 2016). In turn, these stresses are sensitive to the history of rift behavior (Wang and others, 2022), so that the rift state at one point in time directly feeds back to future rifting. Previous studies have also established that rift propagation is sensitive to crucial rift-flank boundary processes such as the transmission of stress between flanks “glued” together by mechanically coherent *mélange* (Larour and others, 2004), backpressure on rift-flank walls from ice *mélange* (Larour and others, 2014, 2021), and contact between flanks (Lipovsky, 2020). However, these studies only examined whether or not a rift would propagate based on the sharp fracture assumption, but did not model the propagation of rifts.

To capture rift propagation and its time-varying effects on ice shelf stresses, we require advanced computational modeling approaches that account for the coupling between ice flow and fracture. Modeling the propagation of rifts and crevasses under the sharp fracture assumption, using the finite element method (FEM) and linear elastic fracture mechanics, introduces algorithmic complexities (Yu and others, 2017). In contrast, continuum damage mechanics combined with the FEM exploits the diffuse fracture assumption and obviates the need for complicated crack tracking algorithms; this simplifies the incorporation of fracture processes within a Stokes-based ice flow model. Recently, damage mechanics based approaches have been used to simulate glacier-scale crevasse propagation (Jiménez and others, 2017; Duddu and others, 2020; Sun and others, 2021; Clayton and others, 2022), and ice-shelf-scale mechanical weakening (Albrecht and

56 Levermann, 2012, 2014; Borstad and others, 2016; Sun and others, 2017) and rift propagation (Huth and
 57 others, 2021b).

58 Here, we develop methods to incorporate rift-flank boundary processes within the computational frame-
 59 work based on anisotropic “creep damage” and vertically integrated ice-shelf flow models (Huth and others,
 60 2021a,b). This quasi-3D (ice-shelf viscous stresses are simulated in the horizontal plane and damage is
 61 evolved in three-dimensional space) framework represents the initiation and time-dependent propagation
 62 of crevasses and rifts. We then investigate how mélange fill, mélange strength, and rift-flank contact influ-
 63 ence the rift path through several parametric sensitivity studies. To demonstrate that the viability of the
 64 proposed framework, we simulate the observed final years of rifting on the Larsen C Ice Shelf that resulted
 65 in the calving of iceberg A-68 in 2017 (Figure 1). The manuscript is organized as follows: in Section 2,
 66 we describe the model equations and rift-flank boundary scheme; in Section 3, we present the parametric
 67 study; in Section 4, we discuss the results; and in Section 5, we offer concluding remarks.

68 2 MODEL EQUATIONS

69 In this section, we summarize the ice-flow model, the anisotropic damage model, and the rift-flank boundary
 70 scheme. All model equations are presented in indicial notation: vectors are notated as $\mathbf{a} = a_i \hat{e}_i$, where i
 71 are the spatial indices of the Cartesian coordinate system $(x_1, x_2, x_3) = (x, y, z)$ and \hat{e}_i are orthonormal
 72 basis vectors; second-order tensors are denoted as $\mathbf{A} = A_{ij} \hat{e}_i \otimes \hat{e}_j$, where \otimes is the dyadic product of
 73 the Cartesian base vectors; and principal values of the tensor are denoted as $\langle A_i \rangle$. We adopt Einstein’s
 74 convention where repeated spatial indices imply summation.

75 2.1 Ice flow model

76 We simulate ice flow with the 2-D Shallow Shelf Approximation (SSA), which is most appropriate for ice
 77 shelves and ice streams that have minimal or no basal drag, so that vertical shear is negligible (Macayeal,
 78 1989; Huth and others, 2021a). The SSA is derived by assuming that the vertical normal stress is equal to
 79 the overburden pressure, neglecting vertical shear stress from the Stokes equations and vertically integrating
 80 and incompressibility, yielding:

$$\frac{\partial M_{ij}}{\partial x_j} - (\tau_b)_i = \rho g H \frac{\partial s}{\partial x_i}, \quad (1)$$

81 where $i, j \in \{1, 2\}$ are the spatial indices in the horizontal $x_1 - x_2$ plane, ρ is the ice density, g is gravitational
 82 acceleration, H is the ice thickness, and s is the surface height above sea level. Parameter $(\tau_b)_i$ is the basal
 83 traction, which is non-zero for grounded ice only, and is described here using a linear friction law

$$(\tau_b)_i = \hat{\beta}^2 v_i, \quad (2)$$

84 where $\hat{\beta}^2$ is a positive basal friction coefficient, and v_i is velocity. In (1), the vertically integrated stress
 85 tensor M_{ij} is defined as

$$M_{ij} = 2\bar{\eta}H (\dot{\epsilon}_{ij} + (\dot{\epsilon}_{11} + \dot{\epsilon}_{22})\delta_{ij}), \quad (3)$$

86 where $\dot{\epsilon}_{ij} = \frac{1}{2} \left(\frac{\partial v_i}{\partial x_j} + \frac{\partial v_j}{\partial x_i} \right)$ is the strain-rate tensor defined as the symmetric gradient of the velocity field
 87 and δ_{ij} is the Kronecker delta. The depth averaged viscosity $\bar{\eta}$ is defined as

$$\bar{\eta} = \frac{1}{2} \bar{B} \dot{\epsilon}_{\text{II}}^{(1-n)/n}, \quad (4)$$

88 where n is the Glen's flow law exponent (Glen, 1955) and $\dot{\epsilon}_{\text{II}}$ is the second invariant of the strain rate
 89 tensor. Herein, we define the depth averaged ice rigidity \bar{B} as

$$\bar{B} = E^{-1/n} \bar{B}_{\text{T}}, \quad (5)$$

90 where E is an enhancement factor commonly associated with fabric variations that can vary spatially in the
 91 horizontal plane. Parameter \bar{B}_{T} is the vertical average of the temperature-dependent ice rigidity $B_{\text{T}}(z)$:

$$\bar{B}_{\text{T}} = \frac{1}{H} \int_b^s B_{\text{T}}(z) dz, \quad (6)$$

92 where b is the ice-shelf draft and $B_{\text{T}}(z)$ is calculated from the depth-varying temperature field $T(z)$ using
 93 the standard Arrhenius relation for ice (Cuffey and Paterson, 2010). The boundary condition at the ice
 94 front is

$$M_{ij} \hat{n}_j = \left(\frac{1}{2} \rho g H^2 - \frac{1}{2} \rho_w g b^2 \right) \hat{n}_i, \quad (7)$$

95 where $\hat{\mathbf{n}}$ is the unit (outward) normal to the ice front and ρ_w is the seawater density. The first and
 96 second terms in the parentheses are the depth integrals of the pressures associated with ice and seawater,
 97 respectively. Because the ice pressure exceeds seawater pressure, this boundary condition acts such that

98 it “pulls” the ice shelf seaward. Appropriate Dirichlet conditions for velocity are enforced at all other
 99 boundaries. We solve the SSA using the finite element routine available in Elmer/Ice (Gagliardini and
 100 others, 2013), which we modify to incorporate damage as described below.

101 2.2 Anisotropic damage model

102 We use an SSA parameterization (Huth and others, 2021b) of the anisotropic creep damage model that was
 103 calibrated for glacier ice according to laboratory tests of ice creep to failure under uniaxial tension (Pralong
 104 and Funk, 2005). Damage gradually accumulates with time according to a stress-based evolution function,
 105 and is incorporated into the vertically integrated momentum balance (1), where it acts to decrease ice
 106 viscosity and increase deformation rates for a given stress. The gradual evolution of damage can represent
 107 micro/meso-scale crack formation to macro-scale brittle fracture driving the propagation of full-thickness
 108 crevasses or rifts, which is consistent with seismic observations (Bassis and others, 2007). We track the
 109 damage variable on the integration points (defined by Gaussian quadrature) within each finite element.
 110 We ignore advection for simplicity, which is justified given the short timescale of our simulations.

111 *Creep damage evolution*

112 Damage is represented as a second-order tensor, \mathbf{D} , which has three real principal values, $\langle D_i \rangle$. Each
 113 principal value represents the ratio of the area of cracks to the originally undamaged area along a principal
 114 plane normal to the respective principal direction, where the value of $\langle D_i \rangle$ ranges from zero for undamaged
 115 ice to a theoretical maximum value of $D_{\max} = 1$ for fully-damaged ice. In practice, D_{\max} must be set less
 116 than one to prevent the ice flow equations from becoming ill-posed. In the SSA formulation, $\langle D_3 \rangle = D_{33}$ is
 117 always aligned with the vertical x_3 axis and the other two principal components lie in the horizontal plane.

118 As described in Pralong and others (2006), a linear transformation between the effective stress $\tilde{\boldsymbol{\sigma}}$ (i.e.
 119 force per unit ice area, ignoring cracks and voids) and the applied stress $\boldsymbol{\sigma}$ (force per unit area of ice,
 120 including cracks and voids) can be defined based on the tensorial damage variable as

$$\tilde{\sigma}_{ij} = \frac{1}{2}(\sigma_{ik}w_{kj} + w_{ik}\sigma_{kj}), \quad w_{ij} = (\delta_{ij} - D_{ij})^{-1}. \quad (8)$$

121 Similarly, an effective strain-rate can be defined as

$$\tilde{\dot{\epsilon}}_{ij} = \frac{1}{2}(\dot{\epsilon}_{ik}w_{kj}^{-1} + w_{ik}^{-1}\dot{\epsilon}_{kj})^D, \quad (9)$$

122 where the superscript ‘D’ refers to the deviatoric part obtained by subtracting the mean of the diagonal
 123 components from each diagonal component of the second-order tensor.

124 The rate of damage accumulation \dot{D}_{ij} can be obtained based on the objective (Jaumann) rate of damage
 125 \mathbf{D} as given by (Pralong and Funk, 2005)

$$\dot{D}_{ij} = \frac{\partial D_{ij}}{\partial t} = f_{ij} + W_{ik}D_{kj} - D_{ik}W_{kj}, \quad (10)$$

126 where t is time, \mathbf{W} is the spin tensor with its Cartesian components $W_{ij} = \frac{1}{2}(\frac{\partial v_i}{\partial x_j} - \frac{\partial v_j}{\partial x_i})$, and \mathbf{f} is the
 127 objective damage rate function

$$f_{ij} = B^* \langle \langle \chi - \sigma_{\text{th}} \rangle \rangle^r \left(w_{kl} \hat{\xi}_k^{(1)} \hat{\xi}_l^{(1)} \right)^k \left(\hat{\xi}_i^{(1)} \hat{\xi}_j^{(1)} \right). \quad (11)$$

128 In the above equation, χ is the Hayhurst’s equivalent stress

$$\chi = \alpha \langle \tilde{\sigma}_1 \rangle + \beta \sqrt{\frac{3}{2} \tilde{\sigma}_{mn}^D \tilde{\sigma}_{mn}^D} + \lambda \tilde{\sigma}_{kk}. \quad (12)$$

129 which weights the damage response based on the maximum (most tensile, with the convention that tension
 130 is positive) effective principal stress (weighted by α), the Von Mises stress (weighted by β), and the effective
 131 hydrostatic stress (weighted by $\lambda = 1 - \alpha - \beta$), where $0 \leq \alpha, \beta, \lambda \leq 1$. Damage accumulation is restricted
 132 to where χ exceeds the stress threshold, σ_{th} , according to the Macaulay brackets $\langle \langle \cdot \rangle \rangle$ in (11), defined as

$$\langle \langle x \rangle \rangle = \begin{cases} x, & \text{if } x \geq 0, \\ 0, & \text{if } x < 0. \end{cases} \quad (13)$$

133 In (11), $\hat{\xi}^{(1)}$ is the eigenvector corresponding to the maximum effective principal stress in the horizontal
 134 $x_1 - x_2$ plane, so that damage only accumulates on the plane normal to the $\hat{\xi}^{(1)}$ direction. The other model
 135 parameters, B^* , r , and k , are empirical constants. All parameter values are listed in Table 1, and their
 136 physical interpretation is described in full in Pralong and Funk (2005) and Duddu and Waisman (2012).

137 *Implementation of damage within the SSA*

138 The SSA only yields vertically integrated deviatoric stresses, whereas damage evolution is defined in terms
 139 of the 3-D Cauchy stress field. Therefore, we approximate the Cauchy stress and calculate damage over

140 21 evenly-spaced vertical layers associated with each 2-D integration point (Fig 2), where we also store
 141 the 3-D temperature field. The vertical average of this 3-D damage field is incorporated into the SSA to
 142 account for damage-induced weakening of ice. Thus, our quasi-3D modeling framework accounts for the
 143 coupling between the 3-D stress field determined from the 2-D ice flow model and the 3-D damage field
 144 describing crevasse and rift propagation.

145 To calculate the Cauchy stress, we first calculate deviatoric stress at the vertical coordinate z of each
 146 layer using the flow law (Glen, 1955)

$$\sigma_{ij}^D(z) = 2\eta(z)\tilde{\varepsilon}_{ij}(z), \quad (14)$$

147 where $\tilde{\varepsilon}(z)$ is determined from (9), and the depth-dependent isotropic viscosity is

$$\eta(z) = \frac{1}{2}E^{-1/n}B_T(z)\varepsilon_{II}^{(1-n)/n}. \quad (15)$$

148 Next, we calculate the Cauchy stress as

$$\sigma_{ij}(z) = \sigma_{ij}^D(z) - p_{\text{eff}}(z)\delta_{ij}, \quad (16)$$

149 where $p_{\text{eff}}(z)$ is an “effective” pressure parametrization that accounts for the opposing seawater pressure
 150 that penetrates into basal crevasses (Keller and Hutter, 2014)

$$p_{\text{eff}}(z) = p_i(z) - p_w(z). \quad (17)$$

151 In the above equation, $p_i(z) = \rho g(s - z) - \sigma_{11}^D(z) - \sigma_{22}^D(z)$ is the ice pressure used to derive the SSA under
 152 the hydrostatic assumption (Greve and Blatter, 2009) and p_w is the basal water pressure. If a layer is
 153 above sea level or is only associated with a surface crevasse (i.e. it is not the basal layer and at least one
 154 deeper layer is undamaged) then $p_w(z) = 0$; else, $p_w(z) = \rho_w g(z_{\text{sl}} - z)$, where z_{sl} is the sea level elevation.
 155 Here, we set $z_{\text{sl}} = 0$.

156 Using these Cauchy stresses, the damage tensor components may be updated on integration point layers
 157 as detailed in Section 2.2. The complete numerical implementation of the 3-D damage update procedure
 158 is described in Huth and others (2021b). It includes a Runge-Kutta-Merson scheme for updating \mathbf{D} ,
 159 adaptive time stepping to restrict large changes in damage between timesteps, and a nonlocal integral
 160 damage scheme (Duddu and Waisman, 2013) that alleviates mesh dependence by spatially smoothing the

161 change in \mathbf{D} each timestep over a nonlocal length scale, l_c . Additionally, we account for rapid damage
 162 growth associated with brittle rupture by setting the maximum principal component of 3-D damage to its
 163 maximum value D_{\max} wherever it meets or exceeds a critical threshold D_{crit} (Duddu and Waisman, 2013).
 164 Subsequent damage evolution on ruptured layers is only allowed through rotation of the damage tensor via
 165 the spin terms in (10).

166 The effect of the 3-D damage field can be incorporated into the vertically integrated SSA stress tensor
 167 using the effective strain rate definition as

$$M_{ij} = \int_b^s 2\eta(z) [\tilde{\epsilon}_{ij}(z) + (\tilde{\epsilon}_{11}(z) + \tilde{\epsilon}_{22}(z))\delta_{ij}] dz. \quad (18)$$

168 However, the above equation rewritten in a simplified form to resemble (3) as

$$M_{ij} = 2\bar{\eta}H \left(\bar{\tilde{\epsilon}}_{ij} + (\bar{\tilde{\epsilon}}_{11} + \bar{\tilde{\epsilon}}_{22})\delta_{ij} \right). \quad (19)$$

169 where the effective strain rate $\bar{\tilde{\epsilon}}$ depends on the depth averaged damage $\bar{\mathbf{D}}$ as

$$\bar{\tilde{\epsilon}}_{ij} = \frac{1}{2}(\dot{\epsilon}_{ik}\bar{w}_{kj}^{-1} + \bar{w}_{ik}^{-1}\dot{\epsilon}_{kj})^D, \quad \bar{w}_{ij} = (\delta_{ij} - \bar{D}_{ij})^{-1}. \quad (20)$$

170 By equating (18) and (19), the expression for the depth averaged damage can be obtained as

$$\bar{D}_{ij} = \frac{\int_b^s D_{ij}(z)B_T(z)dz}{\int_b^s B_T(z)dz}. \quad (21)$$

171 We enforce an additional brittle rupture criterion on the depth averaged damage $\bar{\mathbf{D}}$ to capture rapid damage
 172 growth leading to full opening of a rift. This depth averaged rupture criterion uses a unique critical damage
 173 threshold \bar{D}_{crit} and maximum damage value \bar{D}_{\max} , typically set close to 1. At any integration point, if
 174 $\langle \bar{D}_1 \rangle \geq \bar{D}_{\text{crit}}$ or all vertical layers have ruptured, we update all principal components of $\bar{\mathbf{D}}$ to reflect that the
 175 point has fully failed and now represents a rift. Here, we perform this update by setting $\langle \bar{D}_1 \rangle$ to \bar{D}_{\max} and
 176 the other principal components of $\bar{\mathbf{D}}$ to $\bar{D}_{\max} - 0.05$. This adjustment retains a unique maximum principal
 177 component $\langle \bar{D}_1 \rangle$ that allows us to determine rift orientation, which is required to track rift flank contact
 178 (see Section 3). We also set the gravitational driving stress to zero ($\rho g H \frac{\partial s}{\partial x_i} = 0$) for rifted integration
 179 points.

2.3 Rift-flank boundary scheme

In this section, we discuss the derivation of the rift-flank boundary condition, its implementation within the FEM-SSA framework, and its modification for mechanically coherent mélange. The rift-flank boundary condition accounts for the surface forces arising from the contact between rift-flank walls and the presence of mélange and seawater.

Derivation of rift-flank boundary

We derive the boundary condition for rift-flank walls that takes a similar form to the ice-front boundary condition (7), but also accounts for the pressure on flank walls from ice mélange within the rift (Figure 3a) and full or partial contact between opposite rift-flank walls (Figure 3b). Partial contact can occur, for example, near the top of rifts due to flexure and rotation of rift flanks (De Rydt and others, 2018; Lipovsky, 2020). We denote the mélange thickness as H_m and the corresponding ice mélange draft as

$$b_m = H_m \frac{\rho}{\rho_w}, \quad (22)$$

assuming that ice mélange is in floatation and has the same density as glacial ice. Similarly, we define a thickness of contact between flank walls as H_c , which may also have a portion below sea level, b_c . The depth integrated boundary condition for pressure on the rift-flank walls then takes the form

$$M_{ij} \hat{n}_j = \left[\frac{1}{2} \rho g (H^2 - H_c^2 - H_m^2) - \frac{1}{2} \rho_w g (b^2 - b_c^2 - b_m^2) \right] \hat{n}_i, \quad (23)$$

where mélange cannot co-exist at the same depth as contact between rift flanks. Like the ice-front boundary condition (7), this boundary force is oriented along the outward normal to the rift flank wall. Note that this expression is similar to one derived by Larour and others (2014), except that we introduce the H_c and b_c terms that account for pressure from rift-flank contact. Larour and others (2014) also considered friction between rift flanks, as detected for longitudinal rifts along the shear margins where ice shelves meet the bay walls that constrain them. Because this scenario is not applicable to the lateral rifting of interest on Larsen C Ice Shelf, we do not parameterize friction between flanks here.

201 *Implementation within the FEM-SSA damage framework*

202 Typically, in the FEM framework the rift-flank boundary may be embedded into the mesh as a 1-D interface
 203 (i.e. comprised of the edges of 2-D finite elements). The corresponding boundary condition over a 1-D rift-
 204 flank boundary element can be applied, similarly to the SSA ice-front boundary condition as discussed in
 205 the literature (e.g. Weis, 2001; Greve and Blatter, 2009; Huth and others, 2021a). This involves integrating
 206 (23) over each 1-D boundary element Γ_{rf} so that its contribution to the residual force vector f_{iI} for the
 207 node I is

$$\int_{\Gamma_{\text{rf}}} \phi_I \left[\frac{1}{2} \rho g (H^2 - H_c^2 - H_m^2) - \frac{1}{2} \rho_w g (b^2 - b_c^2 - b_m^2) \right] \hat{n}_i d\Gamma, \quad (24)$$

208 where ϕ_I are the standard nodal basis functions. However, evaluating this integral requires explicitly
 209 defining the 1-D rift-flank boundary and remeshing as the rift propagates. Instead, we evaluate the contri-
 210 butions to the residual force vector over the 2-D rift zone defined by fully-damaged integration points, so
 211 that the internal boundary condition can be enforced at runtime as the rift propagates, without requiring
 212 remeshing. For each 2-D element, we map the contribution of the internal boundary to f_{iI} as

$$\sum_{r=1}^{n_r} -\frac{\partial \phi_I(\mathbf{x}_r)}{\partial x_i} \left[\frac{1}{2} \rho g (H^2 - H_m^2 - H_c^2) - \frac{1}{2} \rho_w g (b^2 - b_m^2 - b_c^2) \right]_I w_r |J_r|, \quad (25)$$

213 where n_r is the number of fully-damaged integration points within the element, \mathbf{x}_r is the spatial coordinates,
 214 w_r is the weight corresponding to the integration point, and $|J_r|$ is the determinant of the Jacobian matrix
 215 for the transformation between local (isoparametric) coordinates and global coordinates. To get an intuitive
 216 sense of the mapping in equation (25), note that it closely resembles (24) if it was converted into a volume
 217 integral with the divergence theorem, and evaluated using Gaussian quadrature. However, the difference is
 218 that here, the bracketed term containing the depth integrals of the pressures from seawater, mélange, and
 219 rift flank contact is written as a nodal term that describe conditions at rift-flank walls. We discuss how we
 220 determine the values of the nodal mélange and contact thicknesses and drafts, used within the bracketed
 221 term of (25), in Section 3.2.

222 A simple example of how (25) enforces the internal rift-flank boundary condition on an ice shelf is given
 223 in Figure 4. The blue and red dots within the grid cells represent fully-damaged (rifted) and undamaged
 224 integration points, respectively, so that there are six fully-rifted elements. The arrows indicate the direction
 225 and magnitude of the total contribution from the internal boundary condition to \mathbf{f} for each node, by
 226 evaluating (25) over all elements. Note that this magnitude decreases as x_1 increases because the ice

227 thickness decreases as x_1 increases. Mélange and rift-flank contact are both absent in this example, so
 228 that there is an open-water boundary condition, and $\bar{D}_{\max} \approx 1$ so that effectively no stress is transmitted
 229 between rift flanks. Recalling that we also remove the gravitational driving stress from rifted integration
 230 points, then the only non-negligible contribution of a rift integration point to the model in Figure (4) is
 231 through (25). In this case, our scheme behaves similarly to an element-deletion scheme for any fully-failed
 232 element, wherein the failed element is removed from the mesh and (24) is applied at the new boundaries
 233 that appear in its place (i.e. the edges that the failed element had shared with non-failed elements). Note
 234 that both our scheme and element deletion schemes require that the rift width, as represented by integration
 235 points, must span at least one element in order to approximate the forces associated with inserting a sharp
 236 crack into the mesh. This requirement is satisfied in the nonlocal damage formulation by using a mesh
 237 resolution that is sufficiently smaller than the characteristic nonlocal damage length, l_c .

238 *Modification for coherent mélange*

239 The above rift-flank boundary scheme can be easily modified to account for mechanically coherent mélange
 240 that transmits stress between flanks. For example, in our Larsen C simulations (see Section 3.3), we
 241 consider decreasing \bar{D}_{\max} in some regions as an *ad hoc* approach to assess the influence of a coherent
 242 mélange, in lieu of implementing a more complicated granular rheological model (e.g. Amundson and
 243 Burton, 2018). Stress transmission between flanks is also possible without mélange, where horizontal
 244 compressive stress could be transmitted between rift flanks that are in contact. While not applicable to
 245 our Larsen C simulations, such a situation could occur if a rift is actively closing. This effect could be
 246 accounted for using tension/compression asymmetry schemes (e.g. Murakami, 1988).

247 **3 SIMULATIONS OF RIFTING ON LARSEN C ICE SHELF**

248 We perform parametric studies on the rift propagation on Larsen C Ice Shelf that led to the calving of
 249 iceberg A68 in 2017. We start from an initial rift configuration that roughly corresponds to its state in late
 250 2014, which was held through early 2015. At this point, the rift had already propagated from Gipps Ice
 251 Rise (GIR), as indicated by the star in Figure 1a marking the rift tip. We run several simulations of the
 252 subsequent rift propagation and ice flow evolution from this initial configuration with and without the new
 253 rift boundary scheme. The simulations with the rift boundary scheme differ in the application of mélange
 254 and flank contact conditions, in order to investigate their role in controlling the rift path. By performing

255 this study on Larsen C Ice Shelf, we also aim to demonstrate that our damage model can simulate observed
 256 rifting. In the following sections, we describe the initial model configuration, the approach used to track
 257 rift-flank contact and assign rift-flank boundary conditions during the simulations, and the setup and
 258 results for each rifting simulation.

259 3.1 Initial configuration

260 To develop the initial model state, we establish the ice geometry, solve for 3-D temperature, and determine
 261 fields for the basal friction coefficient, the enhancement factor, and an initial damage. While our study
 262 focuses on ice shelf processes, the model domain also comprises all grounded ice within the Larsen C ice
 263 sheet-ice shelf system. Inclusion of grounded ice is necessary to capture advection into the ice shelf during
 264 the temperature solution; it is also necessary because rift propagation during the prognostic (i.e. forward-
 265 in-time) simulations can affect ice velocity both throughout the ice shelf and upstream of the grounding
 266 line. We determine the initial ice geometry from satellite observations, as described in Appendix A. We
 267 use the same 0.5 km node spacing for both this initialization procedure and the rifting simulations.

268 We determine a 3-D temperature field as it is required to calculate $B_T(z)$ using the standard Arrhenius
 269 relation for ice and its vertical average \bar{B}_T . Recall that $B_T(z)$ influences the 3-D viscosity field in equation
 270 (15) and \bar{B}_T influences the vertically averaged viscosity through equations (4) and (5). We summarize our
 271 procedure to determine the 3-D temperature field in Appendix B, and the resulting \bar{B}_T field is shown in
 272 Figure 5a.

273 We determine the basal friction coefficient, enhancement factor, and initial damage fields using an
 274 inversion procedure that minimizes mismatch between observed and modeled velocities. The observed
 275 velocities are derived from a smoothed compilation of 2015 Landsat-8 data (Pope, 2016) with minimal
 276 infilling of gaps in coverage using the 2015-2016 MEaSUREs data mosaic (Rignot and others, 2017). In
 277 lieu of an anisotropic inversion scheme, we define the initial damage field as an isotropic, vertically averaged
 278 field \bar{D} , to simply incorporate it into the SSA solution as part of the vertically averaged ice rigidity field,
 279 \bar{B} in (4) (e.g. Borstad and others, 2013, 2016; Sun and others, 2017). Therefore, we express \bar{B} based on
 280 the isotropic vertically averaged damage as

$$\bar{B} = (1 - \bar{D})E^{-1/n}\bar{B}_T. \quad (26)$$

281 We designed our inversion procedure to optimize both the basal friction coefficient $\hat{\beta}^2$ (in grounded

282 regions), and the vertically averaged ice rigidity \bar{B} (e.g. Fürst and others, 2015), with additional treatment
283 to separate the contributions of E and \bar{D} to \bar{B} . While there is no unique solution for how to separate
284 these variables, we aim to determine a \bar{D} field with sharp gradients aligned with observed fractures, and
285 a smoother E field that describes gradual changes to ice fabric over the domain. A consequence of the
286 smooth E field is that during the prognostic simulations, the rift propagates into a region with smooth
287 spatial variations of ice stiffness, which was inferred without overfitting. This effect helps ensure that
288 inferred ice stiffness influences the simulated rift paths less than changing rift-flank boundary treatments
289 between simulations does, so that we can more clearly investigate how these boundary treatments alone
290 affect rifting. We fully describe the inversion scheme in Appendix C, and the relevant \bar{B} , \bar{D} , and E fields
291 are plotted in Figure 5.

292 While the inferred initial damage is 2-D and isotropic, we emphasize that all new damage accumula-
293 tion during the prognostic simulations is 3-D and fully anisotropic, and is incorporated into the SSA as
294 described in Section 2.2. It is possible to convert the inferred 2-D damage into a 3-D field by assuming
295 a vertical distribution of damage, so that the resulting 3-D field can then accumulate additional damage
296 during forward modeling. However, during the prognostic simulations, we do not allow subsequent damage
297 accumulation over areas where non-zero isotropic 2-D damage was inferred, for two reasons: (1) Besides
298 the rifting in question, imagery does not show major changes in fracture on the shelf during our timeframe
299 of interest; and (2) we are only focused on the propagation of the A68 rift into the undamaged ice near
300 the ice front, where we aim to isolate the effect that varying the rift-flank boundary treatments between
301 simulations has on the rift paths. Isolating this effect requires that damage elsewhere on the shelf remains
302 consistent between simulations, as new damage anywhere on the shelf changes stresses throughout the shelf,
303 impacting rifting. Therefore, we disallow subsequent damage evolution in regions with inferred damage,
304 and also in the immediate vicinity of Gipps and Bawden Ice Rises, which are pinning points where changes
305 in damage could substantially influence stress throughout the shelf.

306 Before performing the prognostic simulations, we make two modifications to the initial damage field,
307 which are reflected in Figure 6: First, the inferred damage is unrealistically diffuse so that it does not
308 clearly represent the initial A68 rift, so we redraw it as a sharper rift of fully-damaged points, along which
309 we assess the effects of varying rift flank boundary conditions during the simulations. Second, we initialize
310 an additional region of damage that is observed near the center of the ice front, but not captured during
311 the inversion possibly because it has too minimal of an impact on the smoothed velocity observations.

312 In this region, we assign anisotropic damage corresponding to crevasses oriented normal to the ice flow
 313 direction, i.e. opening in the direction of flow. In agreement with observations (yellow arrow and inset
 314 in Figure 1a), this damage acts to arrest spurious rifting that can otherwise originate from this section
 315 of the ice front due to radial spreading during the prognostic simulations. For each point in this region,
 316 we assign a vertical damage profile described by fully-damaged surface and basal crevasses, separated by
 317 an undamaged region consistent with some thickness of ice that is floating in hydrostatic equilibrium. We
 318 interpolate this profile to the vertical layers of each integration point, where the undamaged thickness is
 319 calculated so that the depth averaged maximum-principal damage at each point equals 0.5.

320 **3.2 Implementation of the rift-flank boundary scheme**

321 Implementing our rift-flank boundary scheme (Section 2.3) within a prognostic, time-varying simulation
 322 requires a method to track the evolution of the rift-flank contact with changes in the rift width. For
 323 the simulations here that use the rift-flank boundary scheme, we initially assign full contact between
 324 flanks for any new rifting. We assume that the flanks gradually separate as the rift widens because
 325 bending effects should cause them to remain in contact near the surface for longer than the base. Other
 326 processes may also contribute to enhanced contact between flanks, such as fully or partially-calved ice
 327 blocks, refreezing of seawater, or perhaps a combination of misalignment of the vertical rift plane with the
 328 z-axis and buoyancy forces (Walker and Gardner, 2019). However, we assume for simplicity that bending
 329 is the primary mechanism of enhanced contact here so that the contact region is always aligned with the
 330 top of the rift flanks and $b_c = \max(-(s - z_{sl} - H_c), 0)$. While the bending of rift flanks is not captured
 331 within the SSA, we approximate its effect here by linearly decreasing the contact thickness as the rift
 332 widens. To do this, we first save the orientation of the rift at full-thickness rupture of an integration point
 333 by setting the maximum principal 2-D damage component, $\langle \bar{D}_1 \rangle$, to \bar{D}_{\max} , while the other principal 2-D
 334 damage components are set to slightly lower values of $\bar{D}_{\max} - 0.005$. As a proxy for rift widening, we track
 335 the accumulated strain, ε_r , in the $\langle \bar{D}_1 \rangle$ direction (i.e. the rift-opening direction) on each rifted integration
 336 point. A new rift point is initially assigned $\varepsilon_r = 0$, and ε_r evolves on subsequent timesteps as

$$\varepsilon_r^{m+1} = \max(\varepsilon_r^m + \dot{\varepsilon}_r^m \Delta t^m, 0), \quad (27)$$

337 where m is the timestep counter and Δt is the size of the timestep. Parameter $\dot{\varepsilon}_r$ is the nonlocal strain rate
 338 in the rift-opening direction at the integration point, calculated as the average of all neighboring integration

339 points within a radius l_c . Without this nonlocal averaging, ε_r^{m+1} tends to increase at the center of the rift
 340 width compared to the edges, potentially causing error in how the pressure on rift flank walls is applied.
 341 Then, we convert ε_r to a fraction of contact, $F_c = \max(1 - \varepsilon_r/\varepsilon_r^{\max}, 0)$, so that contact linearly varies
 342 between 100% at initial full-thickness rupture ($\varepsilon_r = 0$) to 0% when $\varepsilon_r \geq \varepsilon_r^{\max}$. Here, we set $\varepsilon_r^{\max} = 0.04$ for
 343 all simulations. An example ε_r field is given in Figure 7, which is taken from Simulation 3 in Section 3.3.
 344 After calculating F_c , we linearly interpolate it to nodes and calculate the nodal contact thickness in (25)
 345 as $(H_c)_I = (F_c)_I H_I$, as well as the corresponding $(b_c)_I$.

346 The nodal mélange thickness is determined similarly to the thickness of rift flank contact as $(H_m)_I =$
 347 $(F_m)_I H_I$, where F_m is a constant mélange fraction that we assign at specified integration points and
 348 interpolate to nodes. We determine $(b_m)_I$ assuming that the mélange is freely floating. In the simulations,
 349 we never allow mélange and rift flank contact to coexist at the same point, thereby guaranteeing that
 350 mélange and contact thicknesses do not overlap within a vertical rift profile.

351 3.3 Rifting simulations and results

352 We present five prognostic rifting simulations that demonstrate the model performance under different
 353 “what-if” scenarios. The results are reported in Figure 8, where each row (S1–S5) corresponds to one of the
 354 simulations (e.g. row S1 corresponds to Simulation 1). The columns provide a description of the simulation
 355 setup, the rift widening rate ($\dot{\varepsilon}_r$) averaged over 0.01 years (~ 4 days) after the rift begins propagating, and
 356 the final damage fields (i.e. rift paths), upon calving.

357 We describe the motivation, setup, and results for each simulation in the subsections below. Most of
 358 these simulations test either an extreme end-member of range of possible rift-boundary treatments (e.g.
 359 100% vs. 0% mélange fill), or realistic conditions for mélange fill within the rift (e.g. partial mélange
 360 fill that is inviscid vs. mechanically-coherent). Rift treatments are varied between simulations along the
 361 initialized portion of the rift, and in some cases for any newly propagated portion of the rift. However,
 362 all simulations are assigned an open-water (i.e. no mélange) boundary condition for the portion of the
 363 initialized rift that borders Gipps Ice Rise (GIR), which is indicated by the small blue region next to
 364 GIR in the Description column of Figure 8 in row S4. In addition to varying the rift treatment between
 365 simulations, we also assign each simulation a unique damage stress threshold (σ_{th}), set low enough to allow
 366 rift propagation but high enough to avoid excess damage accumulation elsewhere. Adjusting σ_{th} in this way
 367 yields the sharpest and most realistic rifting possible, thereby optimizing each simulation to potentially

368 match the observed rifting. However, if we use the same σ_{th} between all simulations (Supplemental Figure
 369 S1) we obtain similar, but more diffuse, rift paths.

370 **Simulation 1: No rift boundary scheme, $\bar{D}_{\text{max}} \approx 1$**

371 In Simulation 1 (Figure 8, row S1), we implement the damage model without the rift boundary scheme
 372 (except for the open-water boundary next to GIR) and set $\bar{D}_{\text{max}} = 0.995 \approx 1$ so that effectively no stress
 373 is transmitted between rift flanks; this approach is equivalent to implementing the rift boundary scheme
 374 under the end-member assumption that rift flanks are always in contact, or alternatively, always fully-
 375 filled with inviscid mélange that does not transmit stress. This approach is also consistent with many
 376 previous SSA damage models (e.g. Albrecht and Levermann, 2012, 2014; Sun and others, 2017), though
 377 the underlying damage models differ. We set $\sigma_{\text{th}} = 0.7$ MPa, and the rift propagates to the ice front much
 378 more acutely than observed (Figure 1b). Notably, as rift propagation begins, the simulated maximum ice
 379 velocity downstream of the rift is about 80 km/yr while the respective observed velocities (Pope, 2016)
 380 were under ~ 1 km/yr (Figure 5f). The rift widening rate from this simulation is also much greater than
 381 the other simulations below.

382 **Simulation 2: No rift boundary scheme, smaller \bar{D}_{max}**

383 The setup of Simulation 2 (Figure 8, row S2) is identical to Simulation 1 except that we lower \bar{D}_{max} to
 384 0.86 and set σ_{th} to 0.21 MPa. This simulation tests an *ad hoc* approach to controlling rifting by adjusting
 385 \bar{D}_{max} , as performed in a previous study on an idealized geometry (Huth and others, 2021b). Due to the
 386 smaller \bar{D}_{max} , some stress is transmitted between flanks, which restrains the nascent berg from separating
 387 from the ice shelf as quickly as in Simulation 1; at the start of rift propagation, the simulated maximum ice
 388 velocity downstream of the rift is about 1.2 km/yr, greatly reducing the rate of rift widening as compared to
 389 Simulation 1. Simulation 2 yields a final rift path that matches observations more closely than Simulation
 390 1, illustrating this *ad hoc* rift scheme as a simple alternative to the internal rift boundary scheme for
 391 achieving more realistic rift paths. However, the simulated rift path is not as arcuate as the observed rift
 392 path. Furthermore, this *ad hoc* scheme represents rifts by means of “damage softening”, as opposed to
 393 modeling rifts as a discontinuity when using the internal rift flank boundary scheme. This *ad hoc* scheme
 394 lacks a physical interpretation, so tuning to account for specific rift boundary conditions is challenging.

395 **Simulation 3: Rift boundary scheme, no mélange**

396 In Simulation 3 (Figure 8, row S3), we implement the rift boundary scheme with “no mélange” conditions
 397 both within the initialized rift and newly propagated portions of the rift. Thus, this simulation tests the
 398 opposite end-member scenario to Simulation 1. In this case, $\bar{D}_{\max} = 0.995 \approx 1$, and we start the simulation
 399 with 100% rift flank contact at the initialized rift tip that linearly decreases to 0% contact over 30 km from
 400 the tip, as indicated by the black-to-white gradient in the Description column of Figure 8 in row S3. We
 401 also set $\sigma_{\text{th}} = 0.153$ MPa. The simulated maximum ice velocity downstream of the rift at the start of rift
 402 propagation matches observations well, at about 0.9 km/yr, resulting in a slowly widening rift. However,
 403 unlike Simulation 2, essentially no stresses are transmitted between flanks. Instead, these velocities and
 404 widening are smaller compared to Simulation 1 because the open water boundary condition along much of
 405 the rift reduces the net force pulling the flanks apart.

406 **Simulation 4: Rift boundary scheme, weak mélange**

407 Simulation 4 (Figure 8, row S4) tests the effect of a realistic and inviscid mélange. The setup is identical
 408 to Simulation 3 except for two modifications: (1) we permanently assign 40 % inviscid mélange fill where
 409 the initial rift is colored red in the Description column of Figure 8, row S4; and (2) we set $\sigma_{\text{th}} = 0.22$ MPa.
 410 The mélange effectively does not transmit stress because $\bar{D}_{\max} = 0.995 \approx 1$. The inviscid mélange fill
 411 reduces the ability of the rift to resist opening, yielding maximum velocities downstream of the rift at the
 412 start of propagation of around 1.8 km/yr, which is roughly twice the respective observed velocities. This
 413 simulation has an increased rate of rift widening around Gipps Ice Rise as compared to the Simulations
 414 2, 3, and 5 (Figure 8, column 2), which better simulate the observed the rift path. In other words, the
 415 nascent berg is rotating away from Gipps Ice Rise faster. The resulting rift path lies between the end cases
 416 of Simulation 1 (i.e. no rift boundary condition, or 100 % mélange fill that does not transmit stress) and
 417 Simulation 3 (i.e. rift boundary condition with no mélange).

418 **Simulation 5: Rift boundary scheme, mechanically coherent mélange**

419 Simulation 5 (Figure 8, row S5) tests the effect of a realistic and mechanically-coherent mélange. The setup
 420 of this simulation is identical to Simulation 4, except we lower $\bar{D}_{\max} = 0.98$ wherever the 40% mélange
 421 fill is applied and set $\sigma_{\text{th}} = 0.165$ MPa. The usual $\bar{D}_{\max} = 0.995$ is set everywhere else. In the mélange
 422 regions, decreasing \bar{D}_{\max} from 0.995 to 0.98 locally quadruples the minimum ice stiffness, which scales with

423 $(1 - \bar{D}_{\max})$. Thus, the *mélange* can transmit some stress between flanks and acts to “hold” them together.
 424 Simultaneously, the rift pressure boundary condition is active in this simulation, and reduces the net force
 425 pulling the flank walls apart from each other, so long as the rift-flank contact is less than 100%. Thus,
 426 Simulation 5 is a hybrid of Simulations 2, 3, and 4. It achieves velocities downstream of the rift and a rift
 427 path that are consistent with observations.

428 4 DISCUSSION

429 Our results demonstrate how rift flank boundary conditions and *mélange* strength can influence the rift
 430 path. A greater amount of weak (inviscid) *mélange* fill or contact between rift flanks decreases the rift
 431 flank boundary force (23), which is oriented normal and outward to each rift flank. As demonstrated in
 432 Simulations 1 and 4, this effect increases rift-widening rates (i.e. increases velocities downstream of the
 433 rift), especially near Gipps Ice Rise, which diverts the rift path towards the ice front at a more acute
 434 angle than for simulations characterized by smaller rift-widening rates (i.e. smaller downstream velocities).
 435 Smaller rift-widening rates result from the opposite conditions – a lesser amount of weak *mélange* fill or
 436 contact between flanks – or from stronger *mélange* fill that can transmit sufficient stresses between flanks
 437 to slow them from separating. The rift paths in Simulations 3 (“no *mélange*”) and 5 (“strong *mélange*”),
 438 which are associated with smaller rift-widening rates, closely matched the observed rift paths; whereas,
 439 the rift paths for simulations associated with weak *mélange* and increased rift-widening rates (Simulations
 440 1 and 4) did not. Though varying amounts of *mélange* fill were measured within the rift near Gipps Ice
 441 Rise (Larour and others, 2021), we cannot fully confirm that our “strong *mélange*” simulation is the most
 442 accurate representation of the observed rifting, for two reasons: (1) for simplicity, we approximated the
 443 rift system near Gipps Ice Rise as a single rift, but satellite imagery suggests it was actually a system of
 444 two rifts separated by a thin strip of intact ice until calving, which could have contributed to the overall
 445 stress regime of the rift; and (2) The observed *mélange* fill possibly separated from the rift flank walls
 446 or stretched thin as the rift widened, thereby transitioning to the “no *mélange* case” over time, but we
 447 hold *mélange* conditions constant over time. To improve the accuracy of our approach for determining the
 448 processes that drove the Larsen C rifting, we would need to implement the observed complex rift geometry
 449 and spatiotemporally-varying *mélange* conditions.

450 Our simulations only vary *mélange* fill and \bar{D}_{\max} , while holding all other damage and rift-flank boundary
 451 parameters constant. However, there are likely other combinations of these constant parameters that

452 may yield similar modeled rift paths. For example, there is little observational guidance for choosing an
 453 appropriate value for ε_r^{\max} . Nevertheless, only the most extreme values of ε_r^{\max} seem to have a strong
 454 impact on rifting. Setting ε_r^{\max} too close to its lower limit of zero will effectively eliminate rift flank
 455 contact. Such lack of rift flank contact will prevent the rift in the “no mélange” simulation (Simulation 3)
 456 from propagating for any damage stress threshold, σ_{th} . Conversely, setting ε_r^{\max} to a large value effectively
 457 prevents rift flanks from separating, resulting in greatly increased velocities downstream of the rift and
 458 rapid rift propagation, which can influence the rift path like in Simulation 1. In Simulations 3–5, we aimed
 459 to set ε_r^{\max} so that the only effect of rift-flank contact was to consistently enable rift propagation by locally
 460 increasing stress at the rift tip, without excessive flank contact that could noticeably influence the rift
 461 path. This approach allowed us to solely attribute any differences in rift paths between the simulations to
 462 their individual mélange conditions, rather than also having to consider the effects of rift-flank contact on
 463 the rift path.

464 Even though the exact extent of rift flank contact does vary during and between Simulations 3–5, the
 465 resulting influence on rift-widening or velocities downstream of the rift is smaller than that from varying the
 466 mélange conditions between the simulations. For example, as compared to Simulations 3 (“no mélange”)
 467 and 5 (strong mélange), Simulation 4 (“weak mélange”) averages about half the extent of rift flank contact,
 468 but has consistently greater rift-widening rates and velocities downstream of the rift, with roughly twice
 469 as high rift-widening rates at the onset of propagation as shown in Figure 8. Therefore, these rift-widening
 470 rates and downstream velocities must have increased more by the presence of weak mélange in Simulation
 471 4, than decreased by the relatively small extent of rift-flank contact. In fact, it is likely in this case the
 472 extent of rift-flank contact is small because weak mélange increases rift-widening rates and causes rift flanks
 473 to separate and lose contact more quickly.

474 While a range of ε_r^{\max} may be appropriate, decreasing ε_r^{\max} may prevent rifting unless σ_{th} is decreased
 475 as well. Conversely, if increasing ε_r^{\max} , it may be advantageous to increase σ_{th} to prevent excess diffuse
 476 damage from growing around the rift tip. Unfortunately, both the extent of rift-flank contact, as controlled
 477 by ε_r^{\max} in our parameterization, and σ_{th} are poorly constrained. There are few ground penetrating radar
 478 profiles of rift-flank contact available to guide our rift-flank contact parameterization (De Rydt and others,
 479 2018), which are unlikely to be representative of all ice shelves. Moreover, it is not so clear how to even use
 480 radar profiles to calibrate ε_r^{\max} . Another set of potentially poorly constrained parameters are the weights
 481 in the Hayhurst stress criteria, a wide range of whose values seem capable of producing similar results. For

482 example, Figure 9 shows how similar results for Simulation 5 can be obtained when weighting the Hayhurst
483 criteria entirely by the tensile effective stress ($\alpha = 1$), rather than using the Von Mises-dominant weighting
484 that we apply otherwise (Table 1). However, it is possible that the Hayhurst weights may have a more
485 substantial affect on diffuse damage accumulation far from the rift tip, which is typically associated with
486 crevassing. We do not assess this effect here because our focus is on understanding the role of rift-flank
487 boundary conditions on rift propagation.

488 5 CONCLUSIONS

489 We successfully simulated observed rifting in Larsen C Ice Shelf using a combined inverse and forward
490 computational framework, based on vertically integrated viscous ice shelf flow and anisotropic damage
491 formulations. The inversion scheme separates the contributions from damage and the enhancement factor
492 to the inferred ice rigidity. This scheme gives a sharp depth-averaged isotropic damage field that largely
493 resembles observed major rifting and fracture features, and a smoother enhancement factor that may better
494 represent gradual changes in fabric. The results of our rifting simulations lend support for the argument
495 that gravity-driven viscous stress is sufficient to drive rifting consistent with observations, even without
496 including other mechanical processes, such as ice-shelf flexure in response to the impact of ocean swells. We
497 demonstrated that rift-flank contact, mélange thickness, and mélange strength inside rifts can influence the
498 rift path. In our test cases, increased contact or weak mélange resulted in a smaller iceberg, and decreased
499 contact or strong mélange resulted in a larger iceberg.

500 Future studies may consider modifying our inversion procedure to extract anisotropic damage, and
501 convert to 3-D damage according to observed crevasse depths (e.g. from ICESat-2); this could allow further
502 evolution of the inferred damage field within prognostic simulations, which we did not consider herein.
503 Future research must also focus on developing more physically-based and climate-coupled representations
504 of the rift-flank boundary processes, such as a granular rheology model for mélange and a parameterization
505 of how it grows and decays over time based on environmental forcings. Developing these representations
506 and implementing them within our SSA-damage approach would be a major step towards a comprehensive
507 modeling framework that can simultaneously represent ice flow, melt, rifting, and tabular calving. Such
508 a modeling framework would better simulate how ice-shelf weakening may progress, thereby improving
509 projections of ice-sheet evolution and sea-level rise associated with changes in ice-shelf buttressing.

510 **ACKNOWLEDGEMENTS**

511 A. Huth acknowledges support from NSF Office of Polar Programs via grant no. 2139002. R. Duddu and
512 B. Smith acknowledge funding support from NASA Cryosphere award no. 80NSSC21K1003. R. Duddu
513 also acknowledges funding support from NSF Office of Polar Programs via CAREER grant no. PLR-
514 1847173. The statements, findings, conclusions, and recommendations are those of the authors and do
515 not necessarily reflect the views of the National Oceanic and Atmospheric Administration, or the U.S.
516 Department of Commerce. The authors acknowledge GFDL resources made available for this research.

517 **REFERENCES**

- 518 Albrecht T and Levermann A (2012) Fracture field for large-scale ice dynamics. *Journal of Glaciology*, **58**(207),
519 165–176, ISSN 0022-1430 (doi: 10.3189/2012JoG11J191)
- 520 Albrecht T and Levermann A (2014) Fracture-induced softening for large-scale ice dynamics. *Cryosphere*, **8**(2),
521 587–605, ISSN 1994-0416 (doi: 10.5194/tc-8-587-2014)
- 522 Amundson JM and Burton JC (2018) Quasi-static granular flow of ice mélange. *Journal of Geophysical Research:*
523 *Earth Surface*, **123**(9), 2243–2257, ISSN 2169-9003 (doi: 10.1029/2018JF004685)
- 524 Arrigo KR, van Dijken GL, Ainley DG, Fahnestock MA and Markus T (2002) Ecological impact of a large Antarctic
525 iceberg. *Geophysical Research Letters*, **29**(7), 8–1–8–4, ISSN 0094-8276 (doi: 10.1029/2001GL014160)
- 526 Bassis JN, Coleman R, Fricker HA and Minster JB (2005) Episodic propagation of a rift on the Amery Ice Shelf,
527 East Antarctica. *Geophysical Research Letters*, **32**(6), ISSN 0094-8276 (doi: 10.1029/2004gl022048)
- 528 Bassis JN, Fricker HA, Coleman R, Bock Y, Behrens J, Darnell D, Okal M and Minster JB (2007) Seismicity and
529 deformation associated with ice-shelf rift propagation. *Journal of Glaciology*, **53**(183), 523–536, ISSN 0022-1430
530 (doi: 10.3189/002214307784409207)
- 531 Bassis JN, Fricker HA, Coleman R and Minster JB (2008) An investigation into the forces that drive ice-shelf rift
532 propagation on the Amery Ice Shelf, East Antarctica. *Journal of Glaciology*, **54**(184), 17–27, ISSN 0022-1430 (doi:
533 10.3189/002214308784409116)
- 534 Borstad C, Khazendar A, Scheuchl B, Morlighem M, Larour E and Rignot E (2016) A constitutive framework for
535 predicting weakening and reduced buttressing of ice shelves based on observations of the progressive deteriora-
536 tion of the remnant larsen b ice shelf. *Geophysical Research Letters*, **43**(5), 2027–2035, ISSN 0094-8276 (doi:
537 10.1002/2015gl067365)

- 538 Borstad CP, Rignot E, Mouginot J and Schodlok MP (2013) Creep deformation and buttressing capacity of damaged
539 ice shelves: theory and application to Larsen C ice shelf. *Cryosphere*, **7**(6), 1931–1947, ISSN 1994-0416 (doi:
540 10.5194/tc-7-1931-2013)
- 541 Castelnau O, Duval P, Lebensohn RA and Canova GR (1996) Viscoplastic modeling of texture development in
542 polycrystalline ice with a self-consistent approach: Comparison with bound estimates. *Journal of Geophysical*
543 *Research: Solid Earth*, **101**(B6), 13851–13868, ISSN 0148-0227 (doi: 10.1029/96JB00412)
- 544 Clayton T, Duddu R, Siegert M and Martínez-Pañeda E (2022) A stress-based poro-damage phase field model
545 for hydrofracturing of creeping glaciers and ice shelves. *Engineering Fracture Mechanics*, **272**, 108693 (doi:
546 10.1016/j.engfracmech.2022.108693)
- 547 Cuffey KM and Paterson WSB (2010) *The physics of glaciers*. Academic Press, ISBN 008091912X
- 548 Davis PE and Nicholls KW (2019) Turbulence observations beneath Larsen C Ice Shelf, Antarctica. *Journal of*
549 *Geophysical Research: Oceans*, **124**(8), 5529–5550, ISSN 2169-9275 (doi: 10.1029/2019JC015164)
- 550 De Rydt J, Gudmundsson GH, Nagler T, Wuite J and King EC (2018) Recent rift formation and impact on the
551 structural integrity of the Brunt Ice Shelf, East Antarctica. *Cryosphere*, **12**(2), 505–520, ISSN 1994-0416 (doi:
552 10.5194/tc-12-505-2018)
- 553 Duddu R and Waisman H (2012) A temperature dependent creep damage model for polycrystalline ice. *Mechanics*
554 *of Materials*, **46**, 23–41, ISSN 0167-6636 (doi: 10.1016/j.mechmat.2011.11.007)
- 555 Duddu R and Waisman H (2013) A nonlocal continuum damage mechanics approach to simulation of creep fracture
556 in ice sheets. *Computational Mechanics*, **51**(6), 961–974, ISSN 1432-0924 (doi: 10.1007/s00466-012-0778-7)
- 557 Duddu R, Jiménez S and Bassis J (2020) A non-local continuum poro-damage mechanics model for hydrofracturing
558 of surface crevasses in grounded glaciers. *Journal of Glaciology*, **66**(257), 415–429 (doi: 10.1017/jog.2020.16)
- 559 Fürst JJ, Durand G, Gillet-Chaulet F, Merino N, Tavard L, Mouginot J, Gourmelen N and Gagliardini O (2015)
560 Assimilation of Antarctic velocity observations provides evidence for uncharted pinning points. *The Cryosphere*,
561 **9**(4), 1427–1443, ISSN 1994-0424 (doi: 10.5194/tc-9-1427-2015)
- 562 Gagliardini O, Zwinger T, Gillet-Chaulet F, Durand G, Favier L, de Fleurian B, Greve R, Malinen M, Martin C,
563 Raback P, Ruokolainen J, Sacchetti M, Schafer M, Seddik H and Thies J (2013) Capabilities and performance of
564 elmer/ice, a new-generation ice sheet model. *Geoscientific Model Development*, **6**(4), 1299–1318, ISSN 1991-959X
565 (doi: 10.5194/gmd-6-1299-2013)
- 566 Glen JW (1955) The creep of polycrystalline ice. *Proceedings of the Royal Society of London Series A - Mathematical*
567 *and Physical Sciences*, **228**(1175), 519–538 (doi: 10.1098/rspa.1955.0066)

- 568 Greene CA, Gardner AS, Schlegel NJ and Fraser AD (2022) Antarctic calving loss rivals ice-shelf thinning. *Nature*,
569 ISSN 1476-4687 (doi: 10.1038/s41586-022-05037-w)
- 570 Greve R and Blatter H (2009) *Dynamics of Ice Sheets and Glaciers*. Springer Berlin Heidelberg, ISBN 9783642034152
- 571 Haseloff M and Sergienko OV (2022) Effects of calving and submarine melting on steady states and stability of
572 buttressed marine ice sheets. *Journal of Glaciology*, **68**(272), 1149–1166, ISSN 0022-1430 (doi: 10.1017/jog.2022.29)
- 573 Huth A, Duddu R and Smith B (2021a) A generalized interpolation material point method for shallow ice shelves. 1:
574 Shallow shelf approximation and ice thickness evolution. *Journal of Advances in Modeling Earth Systems*, **13**(8),
575 e2020MS002277, ISSN 1942-2466 (doi: 10.1029/2020MS002277)
- 576 Huth A, Duddu R and Smith B (2021b) A generalized interpolation material point method for shallow ice shelves.
577 2: Anisotropic nonlocal damage mechanics and rift propagation. *Journal of Advances in Modeling Earth Systems*,
578 **13**(8), e2020MS002292, ISSN 1942-2466 (doi: 10.1029/2020MS002292)
- 579 Jiménez S, Duddu R and Bassis J (2017) An updated-lagrangian damage mechanics formulation for modeling the
580 creeping flow and fracture of ice sheets. *Computer Methods in Applied Mechanics and Engineering*, **313**, 406–432
581 (doi: 10.1016/j.cma.2016.09.034)
- 582 Jongma JI, Driesschaert E, Fichfet T, Goosse H and Renssen H (2009) The effect of dynamic–thermodynamic
583 icebergs on the Southern Ocean climate in a three-dimensional model. *Ocean Modelling*, **26**(1), 104–113, ISSN
584 1463-5003 (doi: 10.1016/j.ocemod.2008.09.007)
- 585 Joughin I and MacAyeal DR (2005) Calving of large tabular icebergs from ice shelf rift systems. *Geophysical Research*
586 *Letters*, **32**(2), ISSN 0094-8276 (doi: 10.1029/2004gl020978)
- 587 Keller A and Hutter K (2014) Conceptual thoughts on continuum damage mechanics for shallow ice shelves. *Journal*
588 *of Glaciology*, **60**(222), 685–693, ISSN 0022-1430 (doi: 10.3189/2014JogG14J010)
- 589 Larour E, Rignot E and Aubry D (2004) Processes involved in the propagation of rifts near Hemmen Ice Rise, Ronne
590 Ice Shelf, Antarctica. *Journal of Glaciology*, **50**(170), 329–341, ISSN 0022-1430 (doi: 10.3189/172756504781829837)
- 591 Larour E, Khazendar A, Borstad C, Seroussi H, Morlighem M and Rignot E (2014) Representation of sharp rifts and
592 faults mechanics in modeling ice shelf flow dynamics: Application to Brunt/Stancomb-Wills Ice shelf, antarctica.
593 *Journal of Geophysical Research: Earth Surface*, **119**(9), 1918–1935, ISSN 2169-9003 (doi: 10.1002/2014JF003157)
- 594 Larour E, Rignot E, Poinelli M and Scheuchl B (2021) Physical processes controlling the rifting of Larsen C Ice
595 Shelf, Antarctica, prior to the calving of iceberg A68. *Proceedings of the National Academy of Sciences*, **118**(40),
596 e2105080118, ISSN 0027-8424

- 597 Laufkötter C, Stern AA, John JG, Stock CA and Dunne JP (2018) Glacial iron sources stimulate the Southern Ocean
598 carbon cycle. *Geophysical Research Letters*, **45**(24), 13,377–13,385, ISSN 0094-8276 (doi: 10.1029/2018GL079797)
- 599 Lipovsky BP (2020) Ice shelf rift propagation: stability, three-dimensional effects, and the role of marginal weakening.
600 *The Cryosphere*, **14**(5), 1673–1683, ISSN 1994-0424 (doi: 10.5194/tc-14-1673-2020)
- 601 Luckman A, Jansen D, Kulesa B, King E, Sammonds P and Benn D (2012) Basal crevasses in Larsen C Ice Shelf
602 and implications for their global abundance. *The Cryosphere*, **6**(1), 113–123, ISSN 1994-0416 (doi: 10.5194/tc-6-
603 113-2012)
- 604 Macayeal DR (1989) Large-scale ice flow over a viscous basal sediment – Theory and application to Ice Stream-B,
605 Antarctica. *Journal of Geophysical Research-Solid Earth and Planets*, **94**(B4), 4071–4087, ISSN 0148-0227 (doi:
606 10.1029/JB094iB04p04071)
- 607 Martin T and Adcroft A (2010) Parameterizing the fresh-water flux from land ice to ocean with interactive icebergs in
608 a coupled climate model. *Ocean Modelling*, **34**(3-4), 111–124, ISSN 1463-5003 (doi: 10.1016/j.ocemod.2010.05.001)
- 609 Maule CF, Purucker ME, Olsen N and Mosegaard K (2005) Heat flux anomalies in Antarctica revealed by satellite
610 magnetic data. *Science*, **309**(5733), 464–467, ISSN 0036-8075 (doi: 10.1126/science.1106888)
- 611 McGrath D, Steffen K, Scambos T, Rajaram H, Casassa G and Lagos JLR (2012) Basal crevasses and associated
612 surface crevassing on the larsen c ice shelf, antarctica, and their role in ice-shelf instability. *Annals of Glaciology*,
613 **53**(60), 10–18, ISSN 0260-3055 (doi: 10.3189/2012AoG60A005)
- 614 Merino N, Le Sommer J, Durand G, Jourdain NC, Madec G, Mathiot P and Tournadre J (2016) Antarctic icebergs
615 melt over the Southern Ocean: Climatology and impact on sea ice. *Ocean Modelling*, **104**, 99–110, ISSN 1463-5003
616 (doi: 10.1016/j.ocemod.2016.05.001)
- 617 Murakami S (1988) Mechanical modeling of material damage. *Journal of Applied Mechanics*, **55**(2), 280–286, ISSN
618 0021-8936 (doi: 10.1115/1.3173673)
- 619 Pollard D and DeConto RM (2012) Description of a hybrid ice sheet-shelf model, and application to Antarctica.
620 *Geosci. Model Dev.*, **5**(5), 1273–1295, ISSN 1991-9603 (doi: 10.5194/gmd-5-1273-2012)
- 621 Pope A (2016) allenpope/Landsat8_Velocity_LarsenC: Processing Landsat 8 Velocities for Larsen C (doi:
622 10.5281/zenodo.185651)
- 623 Pralong A and Funk M (2005) Dynamic damage model of crevasse opening and application to glacier calving. *Journal*
624 *of Geophysical Research: Solid Earth*, **110**(B1), ISSN 0148-0227 (doi: 10.1029/2004jb003104)

- 625 Pralong A, Hutter K and Funk M (2006) Anisotropic damage mechanics for viscoelastic ice. *Continuum Mechanics*
626 *and Thermodynamics*, **17**(5), 387–408, ISSN 1432-0959 (doi: 10.1007/s00161-005-0002-5)
- 627 Rignot E, Mouginot J and Scheuchl B (2017) MEaSURES InSAR-based Antarctica ice velocity map, version 2 (doi:
628 10.5067/D7GK8F5J8M8R)
- 629 Robin GdQ (1955) Ice movement and temperature distribution in glaciers and ice sheets. *Journal of Glaciology*,
630 **2**(18), 523–532, ISSN 0022-1430 (doi: 10.3189/002214355793702028)
- 631 Sergienko OV (2014) A vertically integrated treatment of ice stream and ice shelf thermodynamics. *Journal of*
632 *Geophysical Research: Earth Surface*, **119**(4), 745–757, ISSN 2169-9003 (doi: 10.1002/2013JF002908)
- 633 Sergienko OV, Goldberg DN and Little CM (2013) Alternative ice shelf equilibria determined by ocean environment.
634 *Journal of Geophysical Research: Earth Surface*, **118**(2), 970–981, ISSN 2169-9003 (doi: 10.1002/jgrf.20054)
- 635 Smith BE, Gourmelen N, Huth A and Joughin I (2017) Connected subglacial lake drainage beneath Thwaites Glacier,
636 West Antarctica. *The Cryosphere*, **11**(1), 451–467, ISSN 1994-0424 (doi: 10.5194/tc-11-451-2017)
- 637 Sun S, Cornford SL, Moore JC, Gladstone R and Zhao L (2017) Ice shelf fracture parameterization in an ice sheet
638 model. *The Cryosphere*, **11**(6), 2543–2554, ISSN 1994-0424 (doi: 10.5194/tc-11-2543-2017)
- 639 Sun X, Duddu R and Hirshikesh H (2021) A poro-damage phase field model for hydrofracturing of glacier crevasses.
640 *Extreme Mechanics Letters*, **45**, 101277 (doi: 10.1016/j.eml.2021.101277)
- 641 Tournadre J, Bouhier N, Girard-Ardhuin F and Rémy F (2016) Antarctic icebergs distributions 1992–2014. *Journal*
642 *of Geophysical Research: Oceans*, **121**(1), 327–349, ISSN 2169-9275 (doi: 10.1002/2015JC011178)
- 643 Van Wessem JM, Reijmer CH, Morlighem M, Mouginot J, Rignot E, Medley B, Joughin I, Wouters B, Depoorter MA,
644 Bamber JL, Lenaerts JTM, Van De Berg WJ, Van Den Broeke MR and Van Meijgaard E (2014) Improved repre-
645 sentation of East Antarctic surface mass balance in a regional atmospheric climate model. *Journal of Glaciology*,
646 **60**(222), 761–770, ISSN 0022-1430 (doi: 10.3189/2014JoG14J051)
- 647 Walker CC and Gardner AS (2019) Evolution of ice shelf rifts: Implications for formation mechanics and morphologi-
648 cal controls. *Earth and Planetary Science Letters*, **526**, 115764, ISSN 0012-821X (doi: 10.1016/j.epsl.2019.115764)
- 649 Wang S, Liu H, Jezek K, Alley RB, Wang L, Alexander P and Huang Y (2022) Controls on Larsen C Ice Shelf retreat
650 from a 60-year satellite data record. *Journal of Geophysical Research: Earth Surface*, **127**(3), e2021JF006346 (doi:
651 10.1029/2021JF006346)
- 652 Weis M (2001) *Theory and Finite Element Analysis of Shallow Ice Shelves*. Phd thesis, Technische Universität
653 Darmstadt

654 Yu H, Rignot E, Morlighem M and Seroussi H (2017) Iceberg calving of Thwaites Glacier, West Antarctica: full-Stokes
655 modeling combined with linear elastic fracture mechanics. *The Cryosphere*, **11**(3), 1283–1296 (doi: 10.5194/tc-11-
656 1283-2017)

657 **APPENDIX A: ICE GEOMETRY**

658 We determine the initial geometry for the Larsen C ice sheet-ice shelf system from satellite observations.
659 We calculate ice shelf thickness from 500 m resolution Cryosat-2 swath-processed surface heights following
660 Smith and others (2017) under the assumption that floating ice is in hydrostatic equilibrium. These surface
661 heights are taken as the mean of available 2009-2017 data, and we subtract firn air content taken as the
662 mean over 2000-2014 as provided in RACMO2.3 (Van Wessem and others, 2014). Ice thickness from the
663 BEDMAP2 compilation (Van Wessem and others, 2014) is used for all grounded ice, as well as for minimal
664 filling of gaps in the Cryosat-2 coverage of floating ice. Note that the initial portion of the rift of interest
665 for the prognostic simulations – extending between Gipps Ice Rise and the star in Figure 1 – is mostly
666 detected in the ice thickness data as a thin region consistent with the presence of sea ice or ice mélange
667 within the rift. However, we replace this region with interpolated thickness from nearby unrifted shelf
668 ice, which is necessary for rift-flank boundary treatment during the prognostic modeling, where we assign
669 seawater pressure and varying amounts of mélange and rift-flank contact as functions of the local ice shelf
670 thickness. Note that this is the only area where we use the rift boundary scheme, though thin ice mélange
671 is also present elsewhere in the domain, primarily between and south of Gipps Ice Rise and the Kenyon
672 Peninsula. While these additional regions are not of interest here, we identify them as having ice thickness
673 under 50 m so that we can exclude them from damage updates, as the damage function is only calibrated
674 for glacial ice.

675 **APPENDIX B: 3-D TEMPERATURE SOLUTION**

676 The temperature solution depends on the same surface velocities used in the inversions (Section 3.1), which
677 is a compilation of 2015 Landsat-8 data (Pope, 2016) with minimal infilling of gaps in coverage using the
678 2015-2016 MEaSURES data mosaic (Rignot and others, 2017). We smooth these velocities considerably
679 for the temperature solution. Based on these velocities, we split our temperature solution into two steps.
680 In Step 1, we calculate the Robin (1955) vertical temperature profile wherever observed surface velocities
681 are under 100 m a^{-1} (“non-SSA” flow). For this solution, we use surface temperature and mass balance

682 calculated from the annual means from 1979-2015 in RACMO2.3 (Van Wessem and others, 2014), and a
 683 geothermal heat flux derived from satellite magnetic measurements (Maule and others, 2005). Step 2 is
 684 the temperature solution wherever observed surface velocities exceed 100 m a^{-1} , where we assume ice flow
 685 is described by the SSA. In these regions, we solve a 2-D, vertically integrated formulation of the heat
 686 advection-diffusion equation for SSA flow (Sergienko, 2014), from which we subsequently approximate a
 687 3-D field. This vertically integrated heat equation takes the form

$$\frac{\partial(\bar{T}H)}{\partial t} = -\frac{\partial(v_i\bar{T}H)}{\partial x_i} + \dot{a}T_s - \dot{b}T_b + \frac{1}{c_p\rho} \left[\kappa_i \left(\left. \frac{\partial T}{\partial x_3} \right|_s - \left. \frac{\partial T}{\partial x_3} \right|_b \right) - W_T H \right], \quad (\text{B1})$$

688 where $\bar{T}H$ is vertically integrated temperature of the ice column with \bar{T} denoting the vertically averaged
 689 temperature, \dot{a} is the surface accumulation/ablation rate (positive for accumulation), \dot{b} is basal melt-
 690 ing/freezing rate (positive for melting), c_p is the heat capacity, κ_i is the thermal conductivity, $W_T = \sigma_{ij}^D \dot{\epsilon}_{ij}$
 691 is internal heating due to ice deformation, T_s and T_b are the surface and basal temperature, respectively,
 692 and $\left. \frac{\partial T}{\partial x_3} \right|_s$ and $\left. \frac{\partial T}{\partial x_3} \right|_b$ are the vertical temperature gradient at the surface and base, respectively.

693 In (B1), we set T_b to pressure melting point for grounded SSA ice and -2° C for floating ice. As for
 694 non-SSA flow, we assign T_s from RACMO2.3 for all SSA regions as well. We also use the RACMO2.3 data
 695 for \dot{a} on the ice shelf, where \dot{b} is then calculated from 2-D SSA mass conservation assuming steady-state
 696 conditions, $\frac{\partial(Hv_i)}{\partial x_i} = \dot{a} - \dot{b}$. We do not follow this same procedure for assigning mass balance rates for
 697 grounded SSA regions as it yields unrealistic basal melting/freezing rates, potentially because: (1) the
 698 fast-flowing grounded ice primarily resides within deep, narrow valleys that are not well-resolved by the
 699 coarse resolution of the surface mass balance dataset; and (2) the SSA assumption that vertical shear is
 700 negligible is an oversimplification in these regions. Instead, for grounded SSA regions, we approximate
 701 $\dot{b} = 0$ under the assumption that grounded basal mass balance is small, and subsequently calculate \dot{a} from
 702 the mass conservation equation. Finally, we set $\left. \frac{\partial T}{\partial x_3} \right|_b = -0.11^\circ \text{ C/m}$ for all SSA regions, and $\left. \frac{\partial T}{\partial x_3} \right|_s = 0$
 703 because observations suggest it should be much smaller in magnitude than $\left. \frac{\partial T}{\partial x_3} \right|_b$. The value for $\left. \frac{\partial T}{\partial x_3} \right|_b$ was
 704 approximated from thermistors frozen into the ice shelf (Davis and Nicholls, 2019), which we assume is
 705 representative of the entire SSA domain because the heat flux should be similar at the base of ice streams
 706 feeding an ice shelf if melting and refreezing is weak (Sergienko and others, 2013).

707 We solve (B1) using the Robin (1955) temperature solution from Step 1, in vertically integrated form, as
 708 an upstream Dirichlet condition. We run 3000 years of vertically integrated temperature evolution, which
 709 is sufficient time to stabilize to a steady state. It is possible for the temperature scheme to yield unrealistic

710 \bar{T} in a few isolated regions, so during the solution, we bound \bar{T} to be greater than the minimum non-SSA
 711 (Robin, 1955) temperature solution along its upstream pathline, and less than -2° C. Such corrections are
 712 not needed near the rifting of interest, and mostly occur for the region south of Kenyon Peninsula and
 713 Gipps Ice Rise where there is a mix of thin ice mélange and calved ice blocks that violate our assumption
 714 of a smooth, steady-state of glacial ice flow.

715 We convert to 3-D temperature field by approximating a vertical temperature distribution at each 2-
 716 D point, which is subsequently interpolated to the same set of 21 vertical layers used to track damage.
 717 Typically, this distribution is a piecewise linear function consisting of a line segment between the ice
 718 surface and midpoint of the ice thickness, and a second line segment between this midpoint and the ice
 719 base. We enforce T_s and T_b at the ice surface and base, respectively. Then, we determine the temperature
 720 at the midpoint so that the resulting temperature function vertically averages to the local value of \bar{T}
 721 from (B1). An exception to this two-segment scheme is when the midpoint temperature falls outside the
 722 same temperature bounds defined above for \bar{T} . In this case, we define a third line segment with constant
 723 temperature equal to the exceeded temperature bound, which is centered at the ice thickness midpoint
 724 and connected at its endpoints to the surface and basal line segments. The length of this third segment is
 725 calculated so that the resulting temperature function vertically averages to the local value of \bar{T} from (B1).

726 APPENDIX C: INVERSION SCHEME

727 Our aim here is to determine the basal friction coefficient field ($\hat{\beta}^2$) in the grounded ice regions, the initial
 728 damage (\bar{D}) field in the floating ice regions, and the enhancement factor field (E). We perform two separate
 729 inversions; we infer the friction coefficient $\hat{\beta}^2$ and extract the initial damage \bar{D} from the first inversion, and
 730 we extract the E field from the second inversion. The first inversion involves simultaneous estimation of
 731 $\hat{\beta}^2$ and \bar{B} that minimizes misfit between observed and modeled velocities. This dual inversion is conducted
 732 as detailed in Fürst and others (2015) using the finite element routines available in Elmer/Ice. It is carried
 733 out by optimizing multiplier fields to initial guesses for $\hat{\beta}^2$ and \bar{B} ; for example, $\bar{B} = \gamma^2 \bar{B}_g$, where γ is the
 734 optimized multiplier field and \bar{B}_g is the initial guess. Following Fürst and others (2015), we use \bar{B}_T and
 735 the local gravitational driving stress as initial guesses for \bar{B} and $\hat{\beta}^2$, respectively. We solve the inversion
 736 several times using different levels of regularization, so that we obtain a range of possible results to choose
 737 from, each with different levels of spatial smoothness in the inferred variables. For each result, we extract

738 an initial damage field wherever the inferred \bar{B} is lower than \bar{B}_T (Borstad and others, 2013) as

$$\bar{D} = 1 - \frac{\bar{B}}{\bar{B}_T}, \quad (\text{C1})$$

739 where \bar{D} must be adjusted so that $0 \leq \bar{D} \leq 1$. We only allow damage on the shelf, as the results for
 740 grounded ice are not reliable due to the uncertainty associated with data errors on mountainous terrain,
 741 the use of a dual inversion, and the indiscriminate use of the SSA throughout the domain. Comparing
 742 the results from different levels of regularization, we select the run with the smoothest solution for \bar{B}
 743 that still captures sharp gradients in the extracted damage field that match visible rifting from satellite
 744 observations. The results on the ice shelf for \bar{B} from this first inversion are given in Figure 5b, and for
 745 the extracted damage field in Figure 5c. The extracted damage captures the observed rifting between the
 746 Kenyon Peninsula and Gipps Ice Rise. Damage is also present around the margins and near the grounding
 747 line, where stresses are elevated and additional bending effects not captured by the SSA can occur as ice
 748 adjusts to floatation. This damage appears to gradually heal as it is advected downstream, likely due to
 749 accumulation of marine ice within basal crevasses (McGrath and others, 2012; Luckman and others, 2012).

750 In the second inversion, we infer \bar{B} alone while incorporating the $\hat{\beta}^2$ and damage from the first inversion
 751 as a constant in the initial guess, that is, $\bar{B}_g = (1 - \bar{D})\bar{B}_T$. Similarly to the first inversion, we run the
 752 second inversion many times with different levels of regularization, where E may be extracted from each
 753 result as

$$E = \left(\frac{\bar{B}}{(1 - \bar{D})\bar{B}_T} \right)^{-n}. \quad (\text{C2})$$

754 We manually choose a result where E is as smoothly varying throughout the domain as possible, while
 755 sufficiently minimizing the mismatch between observed and modeled velocities. We assume that E is
 756 smoothly-varying throughout the domain to represent the gradual transition of fabric orientation from the
 757 shear-based regime of grounded ice to the primarily tensile regime of ice shelves.

758 The results for the overall viscosity parameter, \bar{B} , and the enhancement factor E from this second
 759 inversion are given in Figures 5d and 5e, respectively. The enhancement factor varies from $E \approx 1$ at the
 760 grounding line to $E \approx 0.6$ as ice flows out of inlets into the main cavity of the ice shelf. Further downstream,
 761 E continues to decrease and the minimum values ($E \approx 0.16$) are found under biaxial tension near the ice
 762 front. These values appear to be reasonable when compared to previously-published estimates of ice shelf
 763 enhancement factors associated with fabric orientation. On ice shelves, values for the enhancement factor

764 should generally be taken as less than one to reflect the stiffer girdle-type fabrics that polycrystal models
765 suggest form under tension (Castelnau and others, 1996). One study using an orthotropic flow law (Ma
766 et al., 2010) estimated that an enhancement factor associated with variations in ice fabric under uniaxial
767 tension varies from approximately 1.0 at the onset of ice streams to between 0.5-0.7 for ice shelves.
768 Another study (Pollard and DeConto, 2012) assigned an enhancement factor of 0.3 for ice shelves within
769 an ice sheet-ice shelf model mostly used for paleoclimate studies.

770 While the inversion scheme to separate \bar{B}_T , E , and \bar{D} yields reasonable results, the inferred E and \bar{D} will
771 inevitably account for some other processes that impact \bar{B}_T besides fabric and damage, such as the influence
772 of impurities, missing forces such as mélange or sea ice at the ice front, and errors in data, temperature,
773 and density. Additionally, some damage effects could be captured by the enhancement factor, and vice
774 versa. The damage field extracted from the inversion only identifies the fractures that have a strong impact
775 on the observed ice flow velocity, and does not identify some fractures that appear in imagery (Figure 1).
776 Some of these undetected fractures may have minimal effect on the flow field because, for example, they
777 are shallow or are shielded by surrounding fractures. Given an estimate of crevasse depths (e.g. from
778 ICESat-2), these fractures could potentially be accounted for by increasing \bar{D} , and if necessary, decreasing
779 E accordingly so that the resulting viscosity parameter \bar{B} is the same.

Table 1. Ice and damage parameters common to Simulations 1-5

Parameter	Value	Units
B^*	5.23×10^{-7}	$\text{MPa}^{-r} \text{s}^{-1}$
r	0.43	–
k	4	–
α	0.21	–
β	0.63	–
D_{\max}	0.99	–
D_{crit}	0.5	–
\bar{D}_{crit}	0.8	–
l_c	1	km
ρ_i	917	kg/m^3
ρ_w	1028	kg/m^3
z_{sl}	0	m

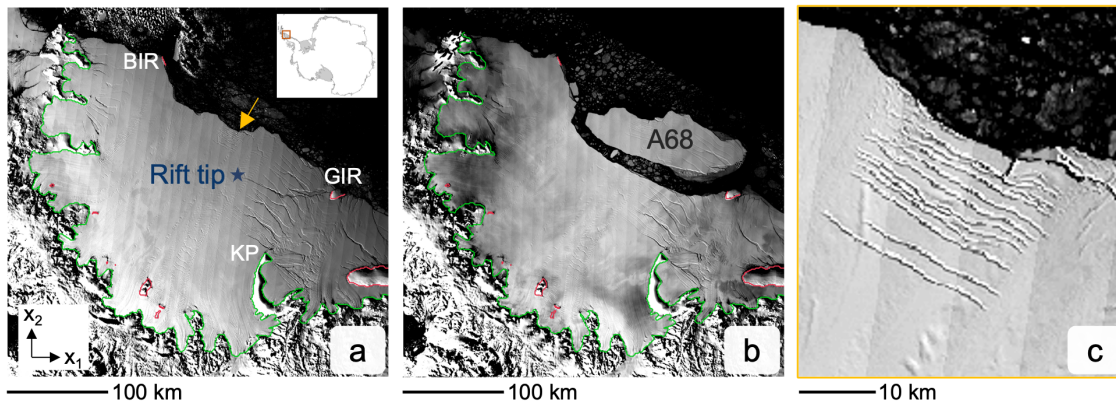


Fig. 1. NASA MODIS images of Larsen C ice shelf on (a) 3 December 2014 and (b) 11 November 2017, 4 months after calving of iceberg A68. The blue star in (a) marks the initial tip position of the rift that propagated to calve iceberg A68. The yellow arrow in (a) indicates a damaged region, shown in detail in (c), that was not captured in the inversion (Figure 5c). BIR = Bawden Ice Rise; GIR = Gipps Ice Rise; KP = Kenyon Peninsula.

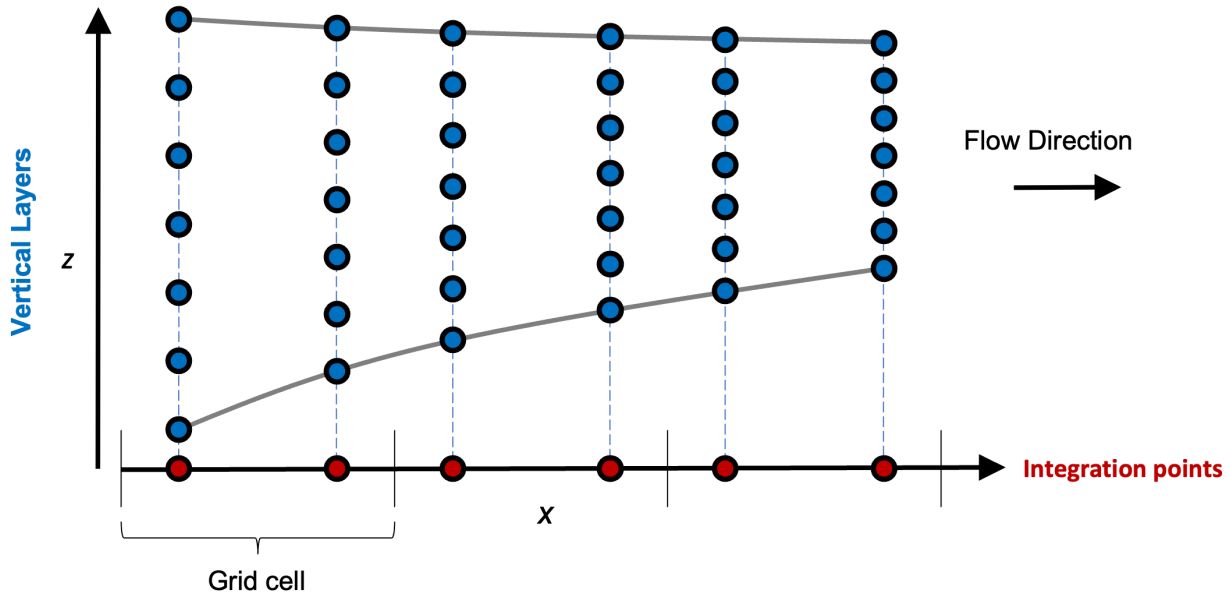


Fig. 2. A flow-line depiction of integration points (red), which are each associated with a series of vertical layers (blue) that are distributed evenly along their thickness. Here, we use 21 vertical layers, where 3-D variables such as damage and temperature are represented.

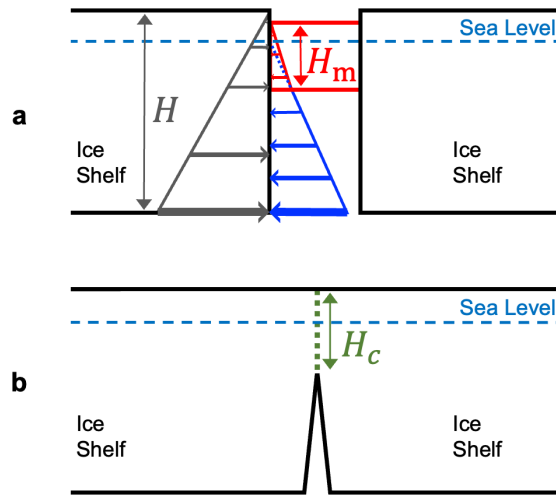


Fig. 3. A schematic of the mechanics within an open rift that are parameterized by the rift-flank boundary condition. (a) The pressures from seawater (blue) and ice mélange (red) with thickness, H_m , partially oppose the pressure from ice shelf rift flanks (gray). (b) Contact between rift flanks over a thickness, H_c , imparts a similar opposing pressure (not shown) to mélange. We assume H_c is always aligned with the rift-flank surface.

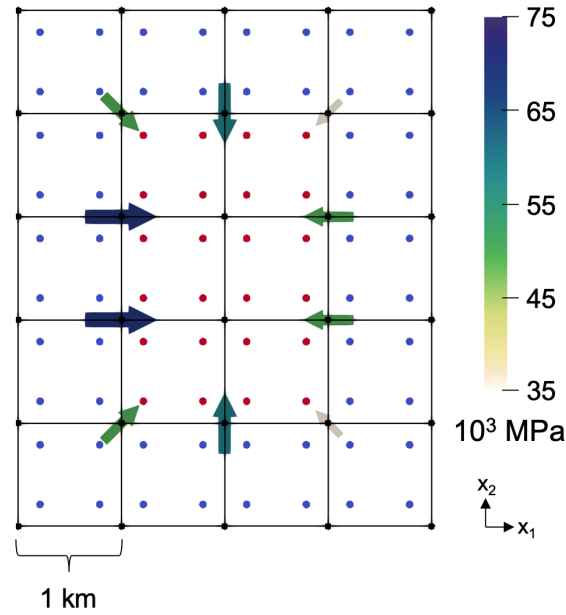


Fig. 4. An example of the direction (arrows) and magnitude (arrow color and size) of the total contribution from the internal rift-flank boundary condition to the nodal residual force vector, by evaluating the mapping in (24) over all elements. Here, the domain is a floating ice shelf where the blue and red dots in the grid cells represent fully-damaged (rifted) and undamaged integration points, respectively. There is no mélange or rift-flank contact in this example, so that the rift flanks have an open-water boundary condition like at the ice front. Ice and seawater density match those given in Table 1. Thickness decreases in the x_1 direction from 410 m at the far left side of the domain to 290 m on the far right side.

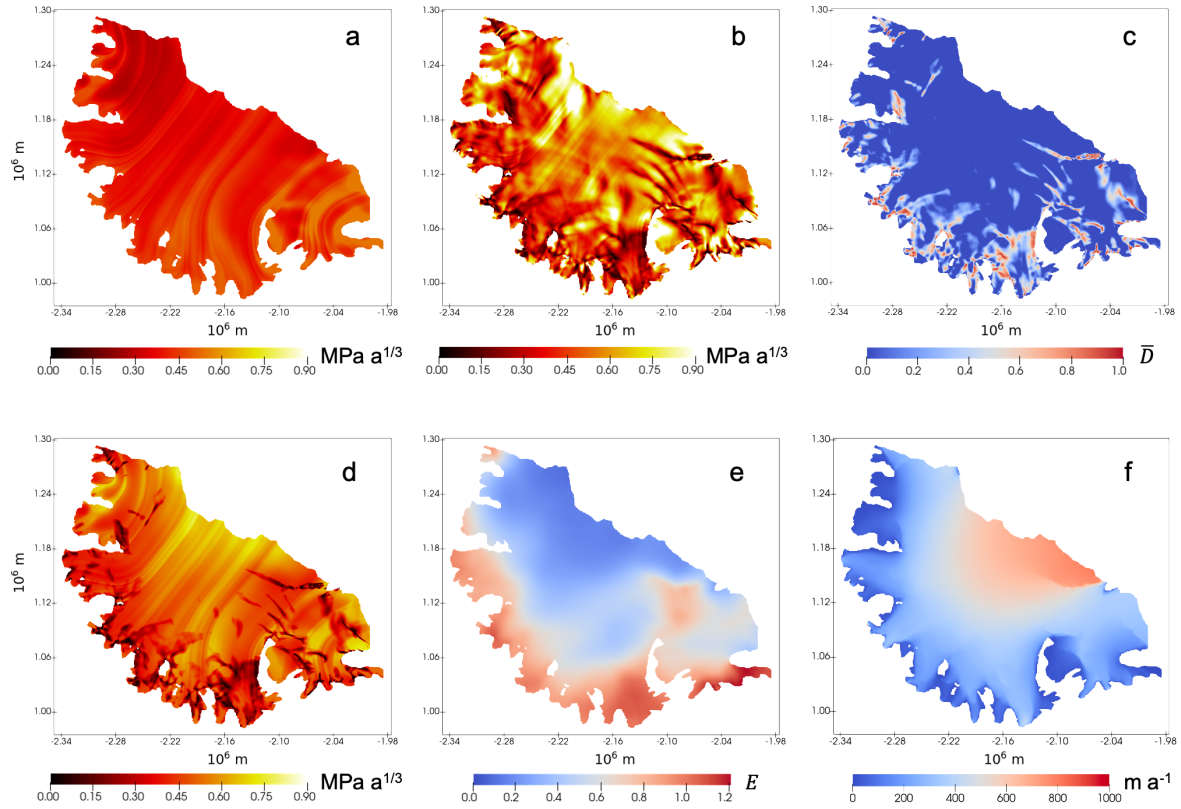


Fig. 5. Results from the inversion scheme used to separate the three field variables contributing to \bar{B} : (a) contribution to \bar{B} from temperature, \bar{B}_T ; (b) \bar{B} from the first inversion; (c) extracted isotropic damage field, \bar{D} ; (d) \bar{B} from the second inversion; (e) extracted enhancement factor, E , and (f) velocity field from the second inversion.

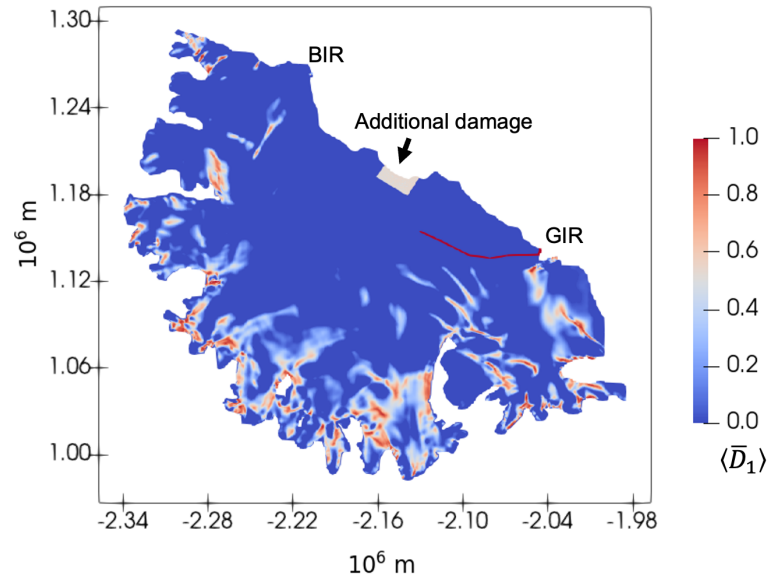


Fig. 6. The initial damage field used in the prognostic model of Larsen C Ice Shelf rift propagation. The redrawn initial rift is plotted here with $\bar{D}_{\max} = 0.995$. The arrow identifies the additional damage initialized along the front. BIR = Bawden Ice Rise. GIR = Gipps Ice Rise.

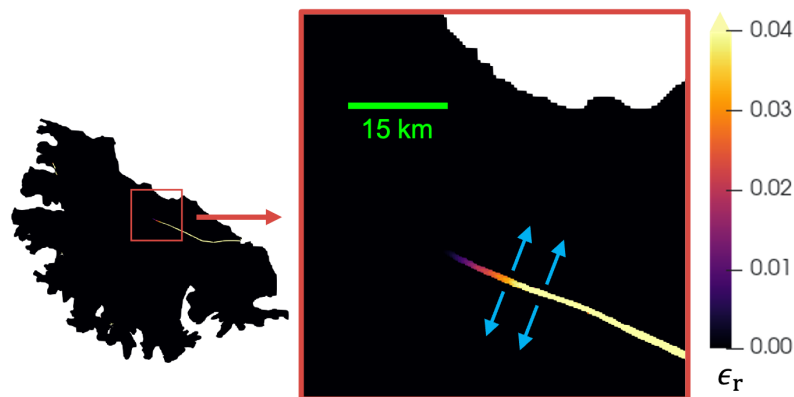


Fig. 7. The accumulated strain, ϵ_r , used as a proxy for tracking rift widening, in the rift-opening direction (blue arrows of inset) as the rift propagates in Experiment 3, with $\epsilon_r^{\max} = 0.04$.

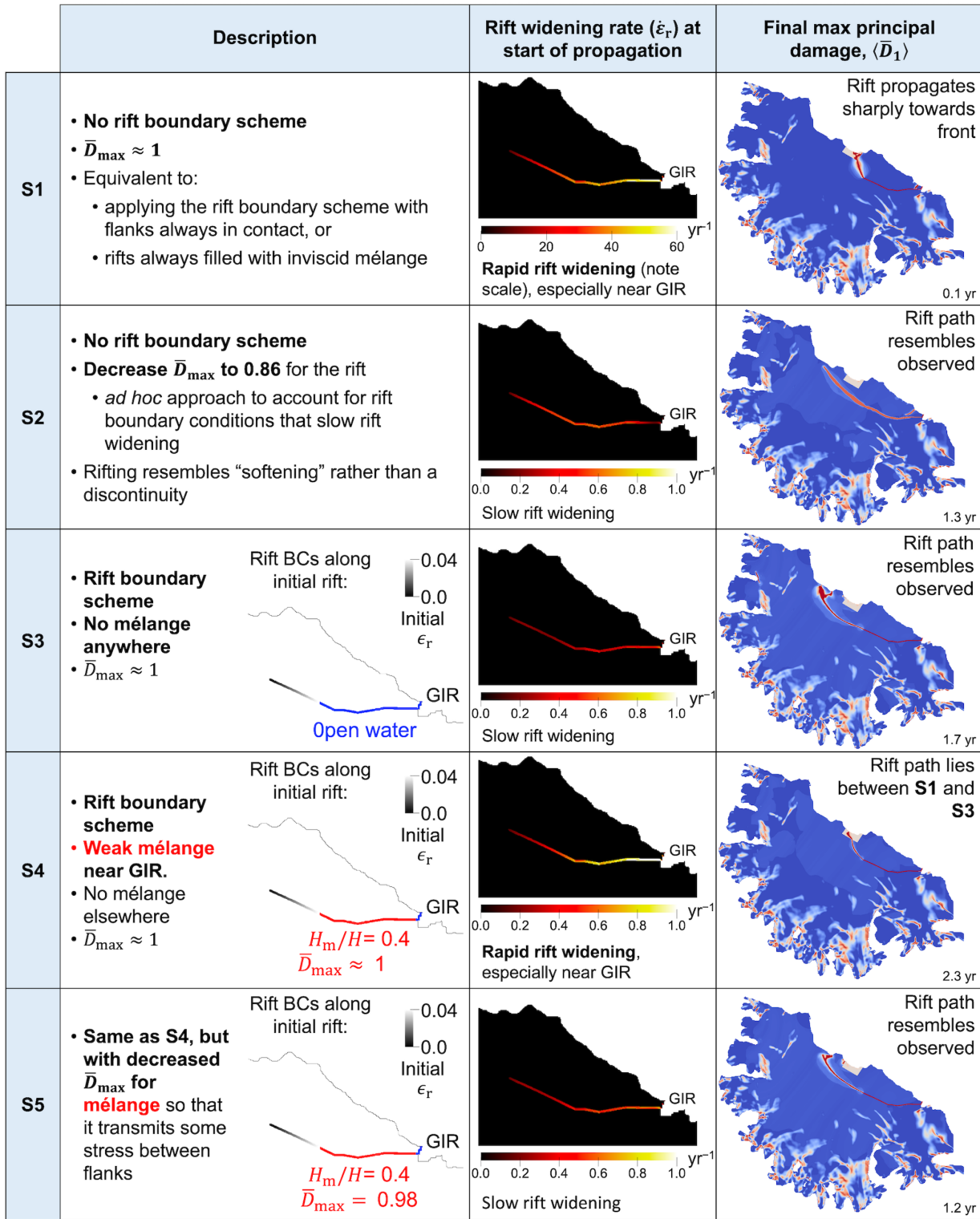


Fig. 8. Results of the five rifting simulations (S1-S5), including (left column) a summary of the initial setup for each experiment; (middle column) the rate of rift widening, $\dot{\epsilon}_r$, averaged over the first 0.01 years of rift propagation; and (right column) the final maximum principal damage fields, $\langle \bar{D}_1 \rangle$, upon calving. Note $\dot{\epsilon}_r$ for S1 is plotted on a different scale than the other simulations. The damage plots use the same legend as Figure 6. GIR = Gipps Ice Rise.

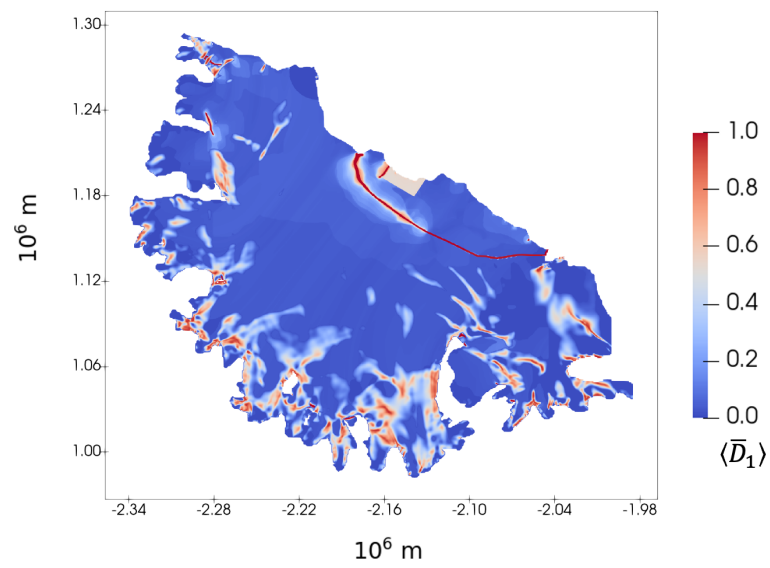


Fig. 9. Final vertically-averaged maximum principal damage field when running simulation 5 (S5) with $\alpha = 1$, $\beta = 0$, and $\sigma_{\text{th}} = 0.099$ MPa.

Supporting Material for “Simulating the processes controlling ice-shelf rift paths using damage mechanics”

Alex HUTH,^{1,4} Ravindra DUDDU,² Benjamin SMITH,³ Olga SERGIENKO⁴

¹ *NOAA/GFDL, Princeton, NJ, USA*

² *Department of Civil and Environmental Engineering, Vanderbilt University, Nashville, TN, USA*

³ *Applied Physics Laboratory, Polar Science Center, University of Washington, Seattle, WA, USA*

⁴ *Atmospheric and Oceanic Sciences, Princeton University, Princeton, NJ, USA*

Contents of this file

Figure S1

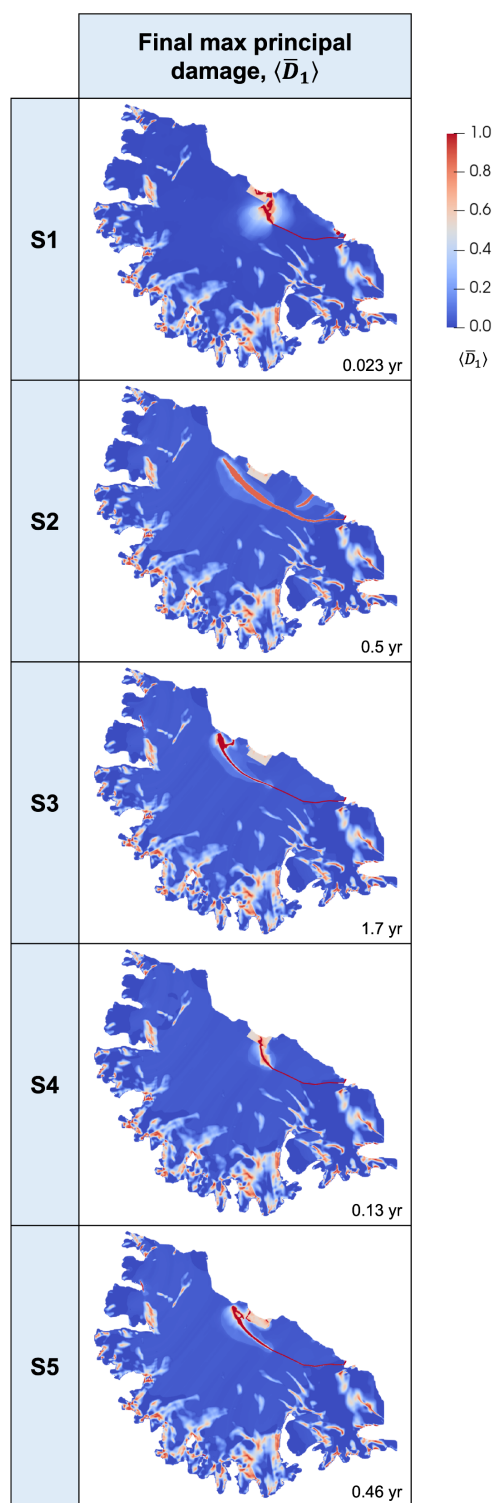


Fig. S1. The final maximum principal damage fields, $\langle \bar{D}_1 \rangle$, upon calving, when running the five rifting simulations with the same damage stress threshold, $\sigma_{th} = 0.153$ MPa. Here, the damage field is not as sharp or well-constrained to the rifting of interest as compared to Figure 8, where σ_{th} is adjusted to allow rifting while minimizing damage accumulation elsewhere. However, the same general rift paths are obtained with either approach.